Vertical Motions in Precipitation Bands in Three Winter Cyclones

MARCIA CRONCE AND ROBERT M. RAUBER

Department of Atmospheric Sciences, University of Illinois at Urbana–Champaign, Urbana, Illinois

KEVIN R. KNUPP

Atmospheric Sciences Department, University of Alabama in Huntsville, Huntsville, Alabama

BRIAN F. JEWETT

Department of Atmospheric Sciences, University of Illinois at Urbana–Champaign, Urbana, Illinois

JUSTIN T. WALTERS AND DUSTIN PHILLIPS

Atmospheric Sciences Department, University of Alabama in Huntsville, Huntsville, Alabama

(Manuscript received and in final form 1 September 2006)

ABSTRACT

The University of Alabama in Huntsville Mobile Integrated Profiling System 915-MHz profiler was deployed in January and February of 2004 to measure vertical air velocities in finescale precipitation bands in winter cyclones. The profiler was placed to sample the "wraparound" quadrant of three winter cyclones in the central and southern United States, and it obtained high-resolution measurements of the vertical structure of a series of bands in each storm. The data revealed bands that were up to 6 km deep, 10–50 km wide, and spaced about 5–20 km apart. Measurements of vertical air motion w within these bands were retrieved from the Doppler spectra using the lower-bound method, adapted to account for the effects of spectral broadening caused by the horizontal wind, wind shear, and turbulence. Derived vertical air motions ranged from -4.3 to 6.7 m s^{-1}, with an uncertainty of about ± 0.6 m s^{-1}. Approximately 29% of the 1515 total derived values were negative, 35% exceeded 1 m s^{-1}, and 9% exceeded 2.0 m s^{-1}. These values are consistent with studies in the Pacific Northwest, except that more extreme values were observed in one band than have been previously reported. There was a high correlation between values of signal-to-noise ratio (SNR) and w within each band ($0.60 \leq r \leq 0.85$), in the composite of bands from each cyclone ($0.59 \leq r \leq 0.79$), and in the overall analysis ($r = 0.68$). The strongest updrafts were typically between 2.0 and 4.0 m s^{-1} and were located near the center of each band in regions of high SNR. Regions of downdrafts within the bands had maximum values between -1.0 and -4.3 m s^{-1} and were typically located along the edges of the bands in regions of low SNR. These results are consistent with snow growth and sublimation processes. The magnitudes of the vertical velocities in the core of the bands were comparable to theoretical predictions for moist symmetric instability (MSI) under inviscid conditions but would appear to be somewhat larger than expected for MSI when turbulent mixing is considered, suggesting that other instabilities, such as potential instability, may have contributed to the band development in these storms.

1. Introduction

Mesoscale precipitation bands often develop in the north and northwest quadrants of extratropical cyclones (Novak et al. 2004). From many studies, it appears that the vertical motions in mesoscale bands are forced by frontogenesis, either in an environment that is stable to upright convection and characterized by small moist symmetric stability (e.g., Thorpe and Emanuel 1985; Sanders and Bosart 1985; Sanders 1986) or in an environment characterized by weak moist symmetric instability (e.g., Bennetts and Sharp 1982; Seltzer et al. 1985; Reuter and Yau 1990; Nicosia and Grumm 1999). Although a significant effort has gone into determining whether moist symmetric instability

Corresponding author address: Robert M. Rauber, Department of Atmospheric Sciences, University of Illinois, 105 S. Gregory St., Urbana, IL 61801.
E-mail: r-rauber@uiuc.edu

DOI: 10.1175/JAM2533.1

is important in band formation, its assessment has generally been difficult (see review by Schultz and Schumacher 1999).

One uncertainty about mesoscale bands is the magnitude of the vertical motions occurring within them. Theoretical calculations of the maximum vertical motion expected in bands formed under inviscid conditions during the release of conditional symmetric instability predict vertical velocities on the order of 1 m s^{-1} (Emanuel 1983; Bluestein 1993, 556–559). Modeling studies of precipitation bands, which include mixing, predict maximum vertical motions during the release of conditional symmetric instability on the order of 10 cm s^{-1} (e.g., Bennetts and Hoskins 1979, 954–957; Knight and Hobbs 1988, their Figs. 8, 11; Xu 1992, p. 637; Persson and Warner 1995, their Fig. 13; Innocentini and dos Santos Caetano Neto 1992, p. 1099; Zhang and Cho 1995, their Fig. 3). However, these predicted values are inherently limited by the models' resolution and subsequent ability to resolve the circulations completely (Knight and Hobbs 1988).

Vertical motions in banded regions of cyclones have been derived directly from measurements made in the northwestern United States during the Cyclonic Extratropical Storms (CYCLES) program (Hobbs et al. 1980; Herzegh and Hobbs 1980, 1981; Houze et al. 1981; Wang et al. 1983; Wang and Hobbs 1983; Locatelli and Hobbs 1987; Hertzman and Hobbs 1988; Hertzman et al. 1988). For example, Herzegh and Hobbs (1980) used a vertically pointing radar to derive maximum velocities of -1 m s^{-1} in downdrafts and $+0.60$ m s^{-1} in updrafts in warm-frontal rainbands, and Houze et al. (1981) used single-Doppler radar analysis to derive maximum vertical motions as large as 0.7–0.9 m s^{-1} in warm-frontal rainbands. The largest vertical velocities reported in this series of papers (± 3 m s^{-1}) occurred in wavelike rainbands near a cold front (Wang et al. 1983). These bands were in the region of potential instability that occurred ahead of the surface occlusion and were almost certainly convective in nature.

Measurements of vertical motions in banded precipitation outside the Pacific Northwest are rare. Sanders and Bosart (1985) studied a snowband associated with a propagating mesoscale gravity wave. They deduced maximum vertical velocities of ~ 1 m s^{-1} from Doppler radar analysis. Rauber et al. (1994) reported maximum vertical velocities in an ice storm of 0.2 m s^{-1} on a 40-km scale. Wolfsberg et al. (1986) calculated the two-dimensional divergence and vertical motion from aircraft data in a banded New England winter storm and estimated the maximum vertical motion to be about 0.15 m s^{-1}. Sienkiewicz et al. (1989) and Geerts and Hobbs (1991) presented dual-Doppler analyses of the vertical motions in a wide cold-frontal and a prefrontal surge rainband within an East Coast cyclone and found vertical velocities between 0.5 and 1.5 m s^{-1}, resolved at a horizontal scale of 1.5 km.

During January and February of 2004, a small field project, Profiling of Winter Storms (PlOWS), was carried out to test the feasibility of using a 915-MHz profiler, a component of the University of Alabama in Huntsville Mobile Integrated Profiling System (MIPS), to measure vertical air velocities in finescale precipitation bands in winter cyclones. The wind profiler was placed in a position to sample the "wraparound" quadrant of three winter cyclones (C1, C2, C3) in the central and southern United States, and it obtained high-resolution measurements of the vertical structure of a series of bands in each storm. The data revealed bands that were up to 6 km deep, 10–50 km wide, and spaced about 5–20 km apart. Measurements of vertical air motion within these bands were retrieved from the zenith Doppler spectra using the "lower-bound method" (LBM; Probert-Jones and Harper 1961; Atlas et al. 1973, p. 28), which in this work is adapted to account for the effects of spectral broadening caused by the horizontal wind, wind shear, and turbulence. The purpose of this paper is to present these measurements. This paper is organized in the following manner. Section 2 presents the method used to obtain the vertical motions within the bands and an uncertainty analysis. Section 3 provides a brief overview of each of the cyclones sampled during the MIPS deployment. Section 4 presents the measurements of vertical motion, and section 5 summarizes the findings.

2. Method

The goal of this project was to use the MIPS Doppler spectra from a 915-MHz Doppler wind profiler to derive vertical air motions w within the bands of winter cyclones. During the project, the profiler was operated in a five-beam mode with a dwell time of 30 s per beam, a gate spacing of 105 m, and 77 range gates per dwell period. The vertical beam was sampled every other dwell period, producing a 67-s time interval between successive vertical beams. There were 128 spectral points in the Doppler spectra, with a Nyquist velocity of 18.16 m s^{-1}. The vertical beam of the profiler had a width of 9°, with the full power at zenith and half-power points at the nominal "edge" of the beam (4.5°), leading to a horizontal resolution at 2-, 4-, and 6-km altitudes of 310, 620, and 940 m, respectively. Because of the wide beamwidth, horizontal and vertical motions of particles in the vertical beam of the profiler both contribute to the radial velocity. The power spectra were produced using a fast Fourier transform applied to the time series

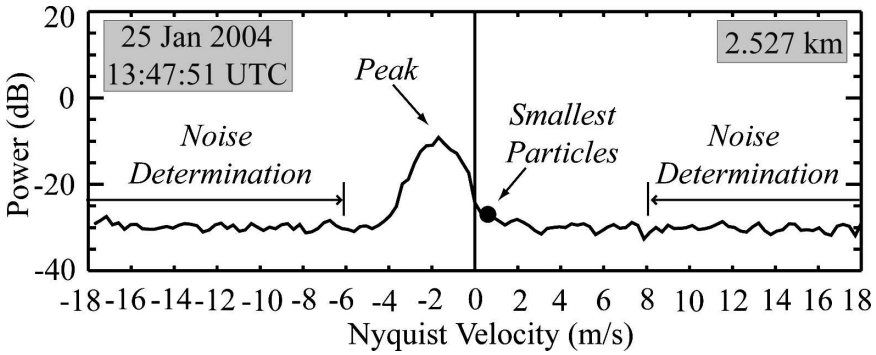

FIG. 1. Doppler power spectrum taken from the 915-MHz Doppler wind profiler at 2.5 km AGL at 1347:51 UTC 25 Jan 2004 in Flora. The dot on the right base of the spectral peak denotes the maximum radial velocity V with a power value of at least two standard deviations above the noise level and is assumed to represent the radial velocity of the smallest particles detectable by the profiler. The average noise power level was determined within the areas bounded by arrows.

of the radial velocity measurements at a specific range. Spectra were analyzed at approximately every 0.5 km at each time interval through several bands in each cyclone.

Figure 1 shows an example of a power spectrum approximately 1 km above the melting layer in a band during C1. Variations in particle radial velocity within the radar measurement volume contribute to the spread of the power spectrum. Such variations are caused by the mean horizontal wind resulting from the 9° beamwidth, vertical shear of the horizontal wind within a range gate, variations in particle terminal fall velocity, and variations in vertical air motion resulting from turbulence (Battan and Theiss 1966; Atlas et al. 1973; Battan 1973; Rogers et al. 1996).

Three Doppler spectral moments [signal-to-noise ratio (SNR), mean radial velocity $\overline{V_r}$, and spectral width] were also derived. SNR is the ratio of the returned signal power to the system noise power. The noise is approximately constant over an operational period, and so variations in SNR when precipitation is present are closely related to variations in precipitation intensity. SNR was not converted to reflectivity factor because the radar constant for the profiler has not been determined.

Estimating vertical air motion from power spectra

The process of retrieving the vertical air velocity used in this paper was first developed by Probert-Jones and Harper (1961) and was adapted by Battan and Theiss (1966). The LBM (Atlas 1964, p. 413; Atlas et al. 1973, p. 28) assumes that the smallest particles detectable by radar have the smallest terminal velocity and are represented as the most positive velocity in the power spectra that is above the noise level (the "smallest particles" point in Fig. 1). Atlas et al. (1973, p. 29) note that "the lower-bound method should work quite well in the case of snow." The method of deriving the vertical air motion from Doppler spectra in this study was adapted from Battan (1973) to account for the effects of spectral broadening resulting from the mean horizontal wind, wind shear, and turbulence (Donaldson and Wexler 1969; Atlas 1964, p. 413).

For a 915-MHz radar, contributions to the total backscatter power (and hence the Doppler spectrum) may arise both from Rayleigh scatter from raindrops and ice particles and from Bragg scatter associated with refractive index inhomogeneities. The LBM can retrieve vertical motion under the condition that the Doppler spectra are produced only from Rayleigh scatter. Bragg scatter contributions, if present, would produce a positive bias in vertical motion values retrieved with the LBM. In the appendix, we show that contributions from Bragg scatter are negligible for the cases examined.

The LBM attempts to determine the radial velocity of the smallest detectable particles within the radar beam. The smallest particles have the lowest terminal velocity and therefore can be assumed to follow the air motion most closely. The smallest detectable particles are represented in the Doppler power spectra at the rightmost point above the noise level (Fig. 1). The first step in the LBM is to determine the radial velocity V at this point.

The mean noise level was determined by calculating the mean of the power in the velocity intervals from +8 to +18.16 m s^{-1} (the positive Nyquist velocity) and −6 to −18.16 m s^{-1} (Fig. 1). These velocity intervals were completely outside the range with powers above the

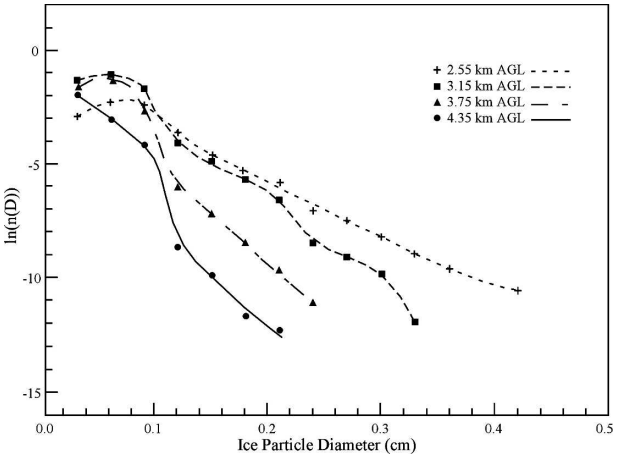

FIG. 2. Snow particle spectra [$n(D)$; cm^{-4}] at four flight altitudes measured in a winter storm over Champaign on 26 Nov 1975 [adapted from Passarelli (1978)].

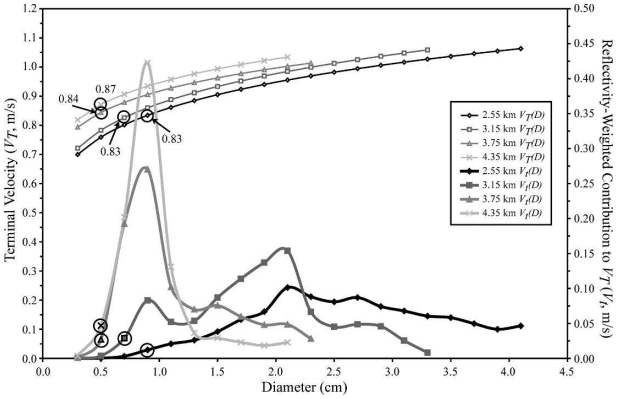

FIG. 3. Terminal velocity V_T (thin lines at top of diagram) and reflectivity-weighted contribution of particles to terminal velocity V_t (thick lines) as a function of diameter for each particle spectrum at the four altitudes in Passarelli (1978). The diameter at each altitude with the smallest nonnegligible contribution to the power returned is highlighted and is circled in the bottom left of the diagram. The corresponding terminal velocity at each altitude is circled and labeled in the top left of the diagram.

noise level for this dataset. The maximum V with a power value at least two standard deviations above the mean noise level was then determined using the following algorithm. The peak of the Doppler spectrum was first identified (Fig. 1). Next, the data point to the right of the peak of the Doppler spectrum that fell below a power value of two standard deviations above the mean noise power level was identified. The velocity at the point to the immediate left of this data point was assigned as V and was used in subsequent calculations to estimate the vertical air velocity using the LBM, with one exception. The MIPS algorithm for acquiring data included ground-clutter suppression, which effectively reduced the power at 0 m s^{-1} to a value below the mean noise in the power spectrum. If the first point to the right of the peak of the Doppler spectrum was at 0 m s^{-1}, the next point to the right was also examined. If the power at this point was greater than two standard deviations above the mean noise power level, then the noise point at 0 m s^{-1} was ignored in the determination of V.

Although the particles contributing to the power at velocity V are the smallest and most closely follow the air motion, they have a nonzero terminal velocity. To estimate w, their terminal velocity must be taken into account. There were no aircraft measurements of particle size distributions or habits collected within the precipitation bands during this study. To estimate particle terminal velocities, measurements taken from similar bands in a winter storm reported by Passarelli (1978) were used.

Figure 2 shows particle size spectra at four flight altitudes sampled by Passarelli during a period of moderate to heavy snowfall over Champaign, Illinois, on 26 November 1975. The spectra were derived from data collected with an optical array precipitation spectrometer. Passarelli, using a precipitation particle camera, primarily observed aggregates of side plane–type crystals at the 4.35-km (−20°C) and 3.75-km (−17°C) altitudes and dendritic-type aggregates at the 3.15-km (−15°C) and 2.55-km (−12°C) altitudes. Terminal velocity–diameter relationships developed by Locatelli and Hobbs (1974) for side plane–type aggregates,

$$V_{0_s} = 0.82D^{0.12}, \tag{1}$$

and dendritic-type aggregates,

$$V_{0_d} = 0.8D^{0.16}, \tag{2}$$

with the density correction factor from Foote and du Toit (1969),

$$V_T(D) = V_0(D)(\rho_0/\rho)^{0.4}, \tag{3}$$

were applied to estimate the fall velocities of the ice particles observed by Passarelli. Data reported by Locatelli and Hobbs (1974) were used to calculate the air density ρ_0 at their measurement site, and the nearest sounding to the profiler was used to calculate the air density ρ at the four altitudes corresponding to the Passarelli study.

The reflectivity-weighted contribution of particles to the terminal fall velocity within the size bin ΔD,

$$V_t(D) = \frac{n(D)D^6V_T(D)\Delta D}{\sum n(D)D^6\Delta D}, \tag{4}$$

was then determined for each of the size spectra in Passarelli (Fig. 3). Figure 3 shows that the smallest-

sized ice particles that had a nonnegligible contribution to the power in the Doppler spectrum ranged in diameter from 0.5 to 0.9 cm. The curves in the upper part of the figure show the terminal velocities of the particles at the four altitudes observed by Passarelli as a function of diameter. The smallest detectable particles $V_{T_{\min}}$ at the four altitudes had terminal velocities between 0.83 and 0.87 m s^{-1}. We chose a single, conservative value of 0.8 m s^{-1} to estimate the terminal velocities of the smallest particles detected by the profiler at all altitudes between the top of the bands and 1 km above the melting level, because the range of snowflake fall speeds is narrow (Atlas et al. 1973).

Figure 4a shows the geometry of the MIPS profiler vertical beam. Because of the 9° beamwidth, there is a contribution to the radial velocity by the mean horizontal wind that contributes to broadening of the power spectrum. The greatest contribution to the radial velocity comes from particles near the edge of the beam (Fig. 4b). Further broadening is induced if vertical shear of the horizontal wind is present, because the radial velocity of the particles near the edge of the beam will vary across a range gate. Last, turbulence induces variations in the vertical motion field, which further broadens the power spectrum.

To account for each of these factors, we took the following approach. The wind speed $\bar{u}$ and vertical shear of the horizontal wind u' at each range gate were determined through temporal interpolation of three soundings (1200, 1800, and 0000 UTC 25–26 January 2004) taken at Lincoln, Illinois (KILX), for C1. For C2, these parameters were determined through temporal and spatial interpolation of the 1200 and 0000 UTC 15–16 February 2004 soundings from Nashville, Tennessee (KBNA), Peachtree City, Georgia (KFFC), and Shelby County Airport near Birmingham, Alabama (KBMX). The winds for C3 were determined from the same sounding locations but using the 1200, 0000, and 1200 UTC 25–26 February 2004 soundings. Select soundings are shown in section 3. Before using the rawinsonde-derived winds, we experimented with using the winds derived from the off-zenith (23°) beams of the profiler. Because of the low power returned from ice particles or clear air outside the bands, long averaging periods were required to determine the winds. However, these long time periods incorporated times for which the precipitation was not uniform across all beams. These inhomogeneities in the precipitation field at the levels of interest led to large uncertainties in the recovered winds and, as a result, derived vertical motions that were often physically implausible. For this reason, we chose to use the rawinsonde-derived winds. The uncertainties in the recovery of vertical motion

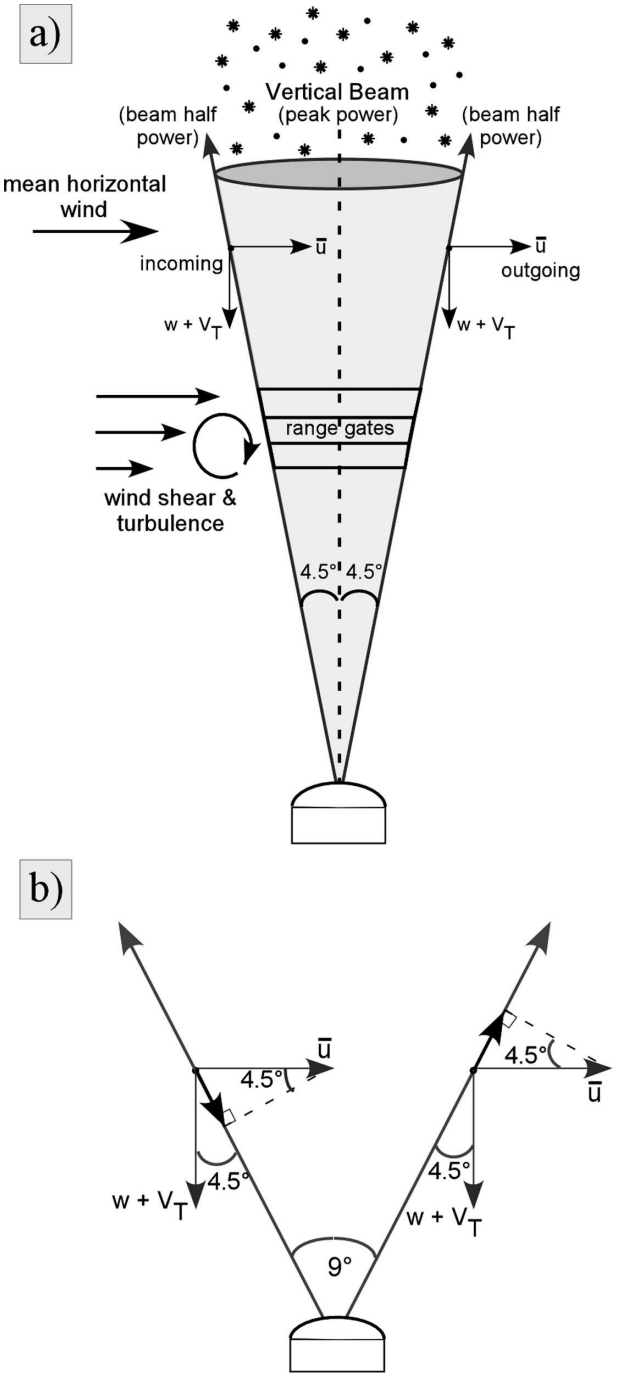

FIG. 4. (a) Schematic diagram of geometry of vertical beam of profiler with beamwidth of 9° and half-power points at edges of beam (4.5° off zenith). Variations in particle terminal fall velocity V_T, mean horizontal wind $\bar{u}$ due to the finite beamwidth, vertical shear of the horizontal wind within a range gate, and variations in vertical air motion resulting from turbulence contribute to broadening of the power spectrum. (b) Geometry of the profiler's vertical beam illustrating the contribution of the (left) incoming and (right) outgoing mean horizontal wind $\bar{u}$, vertical air motion w, and terminal fall velocity V_T to the radial velocity.

TABLE 1. Uncertainties (m s^{-1}) in estimation of w.

	$\Delta V \sec\theta$	$\Delta\theta V \sec\theta \tan\theta$	$\Delta\overline{u} \tan\theta$	$\Delta\theta\overline{u} \sec^2\theta$	$\Delta u' \tan\theta$	$\Delta\theta u' \sec^2\theta$	$\Delta V_{T_{\min}}$	$\Delta w'$	Δw
C1	0.14	0.00	0.46	0.22	0.02	0.00	0.10	0.24	0.6
Band A	0.14	0.00	0.51	0.13	0.01	0.00	0.10	0.18	0.6
Band B	0.14	0.00	0.43	0.21	0.02	0.00	0.10	0.23	0.6
Band C	0.14	0.00	0.47	0.27	0.02	0.00	0.10	0.27	0.6
C2	0.14	0.00	0.57	0.36	0.01	0.00	0.10	0.15	0.7
Band D	0.14	0.00	0.63	0.36	0.01	0.00	0.10	0.15	0.8
Band E	0.14	0.00	0.63	0.36	0.01	0.00	0.10	0.15	0.8
Band F	0.14	0.00	0.47	0.36	0.01	0.00	0.10	0.15	0.6
C3	0.14	0.00	0.44	0.18	0.02	0.00	0.10	0.23	0.6
Band G	0.14	0.00	0.26	0.13	0.01	0.00	0.10	0.15	0.4
Band H	0.14	0.00	0.48	0.20	0.03	0.00	0.10	0.32	0.6
Band I	0.14	0.00	0.46	0.19	0.02	0.00	0.10	0.21	0.6
Overall	0.14	0.00	0.50	0.26	0.02	0.00	0.10	0.20	0.6

using the rawinsonde winds are addressed below. Last, to estimate the turbulence we assumed that the vertical wind fluctuations can be scaled with the vertical shear of the horizontal wind (Rogers et al. 1996), because vertical wind shear will induce tumbling motions in air.

With these assumptions, we can write the maximum radial velocity V at the edge of the profiler beam associated with smallest detectable particles as

$$V = (\overline{u} + u')\sin\theta + (w + w' + V_{T_{\min}})\cos\theta, \quad (5)$$

where $\overline{u}$ is the horizontal wind at the center of each range gate; $u' = (\partial u/\partial z)(\Delta z/2)$, where $\partial u/\partial z$ is the wind shear and Δz is the gate spacing (105 m); θ is equal to 4.5°, the half-beamwidth of the profiler vertical beam; and w' is the maximum variation in vertical velocity associated with turbulence, which is assumed to be equal to u'. Solving for w, we obtain

$$w = \frac{V - (\overline{u} + u')\sin\theta}{\cos\theta} - V_{T_{\min}} - w'. \quad (6)$$

Equation (6) reduces to Eq. (3) in Battan (1973) for the case of an infinitely small beamwidth in which the horizontal wind has no effect on w.

The uncertainty in the estimation of w is given by

$$\Delta w = [(\Delta V \sec\theta)^2 + (\Delta\theta V \sec\theta \tan\theta)^2 + (\Delta\overline{u} \tan\theta)^2 + (\Delta\theta\overline{u} \sec^2\theta)^2 + (\Delta u' \tan\theta)^2 + (\Delta\theta u' \sec^2\theta)^2 + (\Delta V_{T_{\min}})^2 + (\Delta w')^2]^{1/2}. \quad (7)$$

The root-mean-square (rms) estimate of the uncertainties ΔV, $\Delta\overline{u}$, $\Delta u'$, $\Delta V_{T_{\min}}$, $\Delta w'$, and $\Delta\theta$ were determined in the following manner. The variable $\overline{u}$ was determined from spatial and temporal interpolation of the wind speed u from soundings, assuming linearity. At worst, $\overline{u}$ could have had the value u of any of the soundings bounding the interpolation. The uncertainty $\Delta\overline{u}$ was therefore determined by considering the rms difference between the interpolated value of $\overline{u}$ and each of the measured u from all of the soundings used in the interpolation. The uncertainty $\Delta u'$ was determined in a similar way, except considering the sounding values of wind shear within the distance of a range gate. The uncertainty $\Delta w'$ was assumed to equal $\Delta u'$. The uncertainty ΔV was assumed to be the half-width of a spectral bin, 0.14 m s^{-1}. The uncertainty $\Delta V_{T_{\min}}$ based on the calculation of the terminal velocity of the smallest detectable particles was estimated to be 0.1 m s^{-1}. The uncertainty $\Delta\theta$ was assumed to be 1°. These uncertainties were determined for each individual band, because the sounding winds were different in each cyclone. Table 1 summarizes the values of the variables involved in the calculation of the uncertainty in vertical motion, and Δw for each of the nine bands, each cyclone, and the complete analyzed dataset. The uncertainty Δw ranged from 0.4 to 0.8 m s^{-1}, with the overall Δw for the entire dataset equal to 0.6 m s^{-1}.

3. Overview of the storms

This section provides a brief overview of the three cyclones sampled during January and February of 2004. The first sampling period (C1) took place in Flora, Illinois, between 1200 and 2300 UTC 25 January 2004. The cyclone developed east of the Rocky Mountains and tracked eastward across the central and southeastern United States. The latter two cyclones developed near the coast of the Gulf of Mexico and moved northeastward over the southeastern United States. The MIPS was deployed in Huntsville, Alabama, during these two sampling periods, which took place from 0000 UTC 15 February to 0000 UTC 16 February 2004 (C2) and from 1600 UTC 25 February to 1200 UTC 26 February 2004 (C3).

Figures 5 and 6 show the 700-hPa potential tempera-

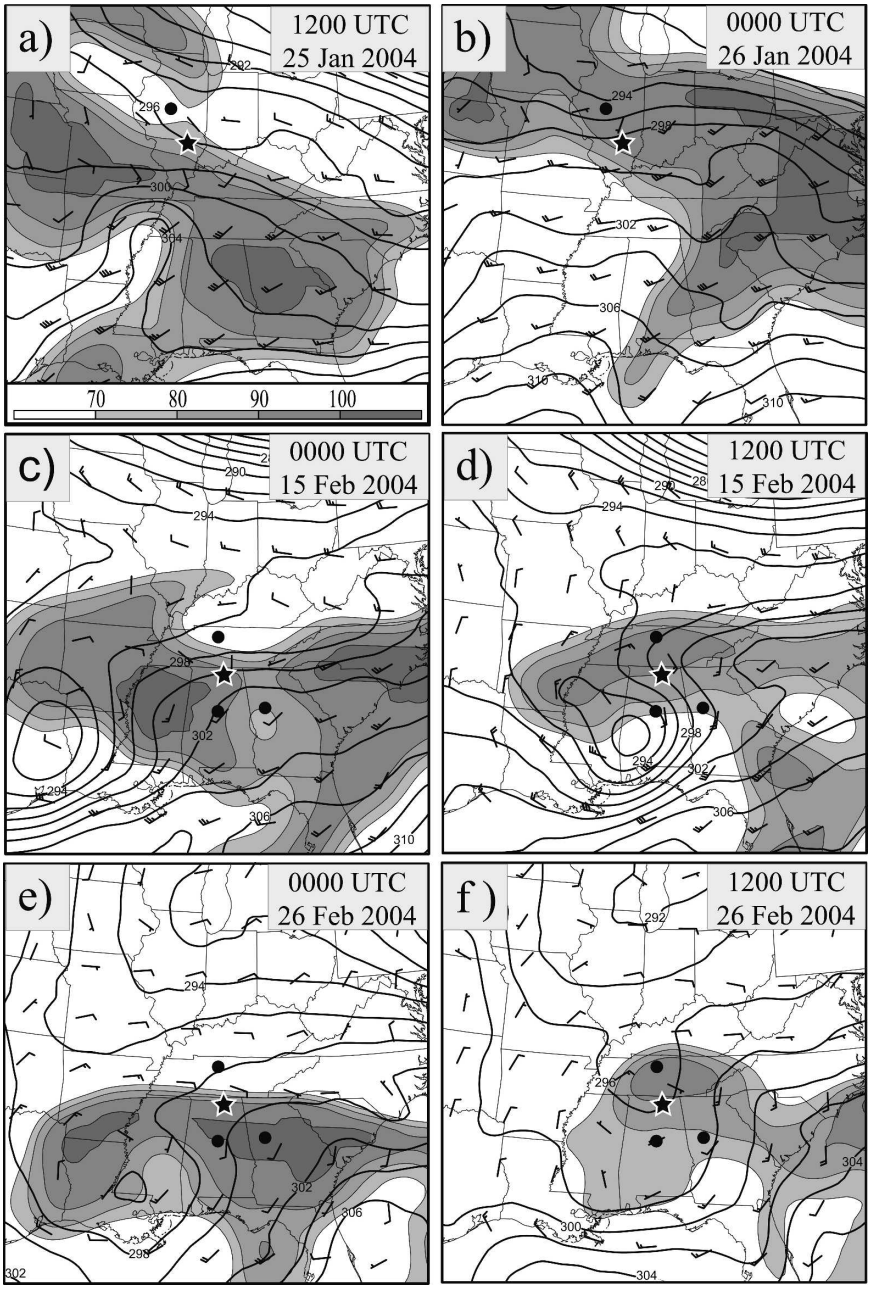

FIG. 5. Eta analysis of potential temperature (heavy contours; 2-K intervals), relative humidity (shaded; 10% intervals greater than 70%), and winds (one full barb is 10 m s^{-1}) at 700 hPa for C1 at (a) 1200 UTC 25 and (b) 0000 UTC 26 Jan 2004, C2 at (c) 0000 and (d) 1200 UTC 15 Feb 2004, and C3 at (e) 0000 and (f) 1200 UTC 26 Feb 2004. The relative humidity scale is in (a). The star depicts the profiler location and the dots denote sounding locations.

ture θ and equivalent potential temperature θ_e, respectively, with relative humidity >70% shaded, for two times during each cyclone. A regional composite radar image at the time of each event, in the vicinity of the MIPS location for each cyclone, appears in Fig. 7. Figure 8 shows the SNR from the profiler in the left column and mean radial velocity $\overline{V}_r$ in the right column. The minimum radial velocities were located consistently below the melting layer during each cyclone and represent faster-falling precipitation in the form of rain or freezing rain. Figure 9 shows relevant soundings for each cyclone.

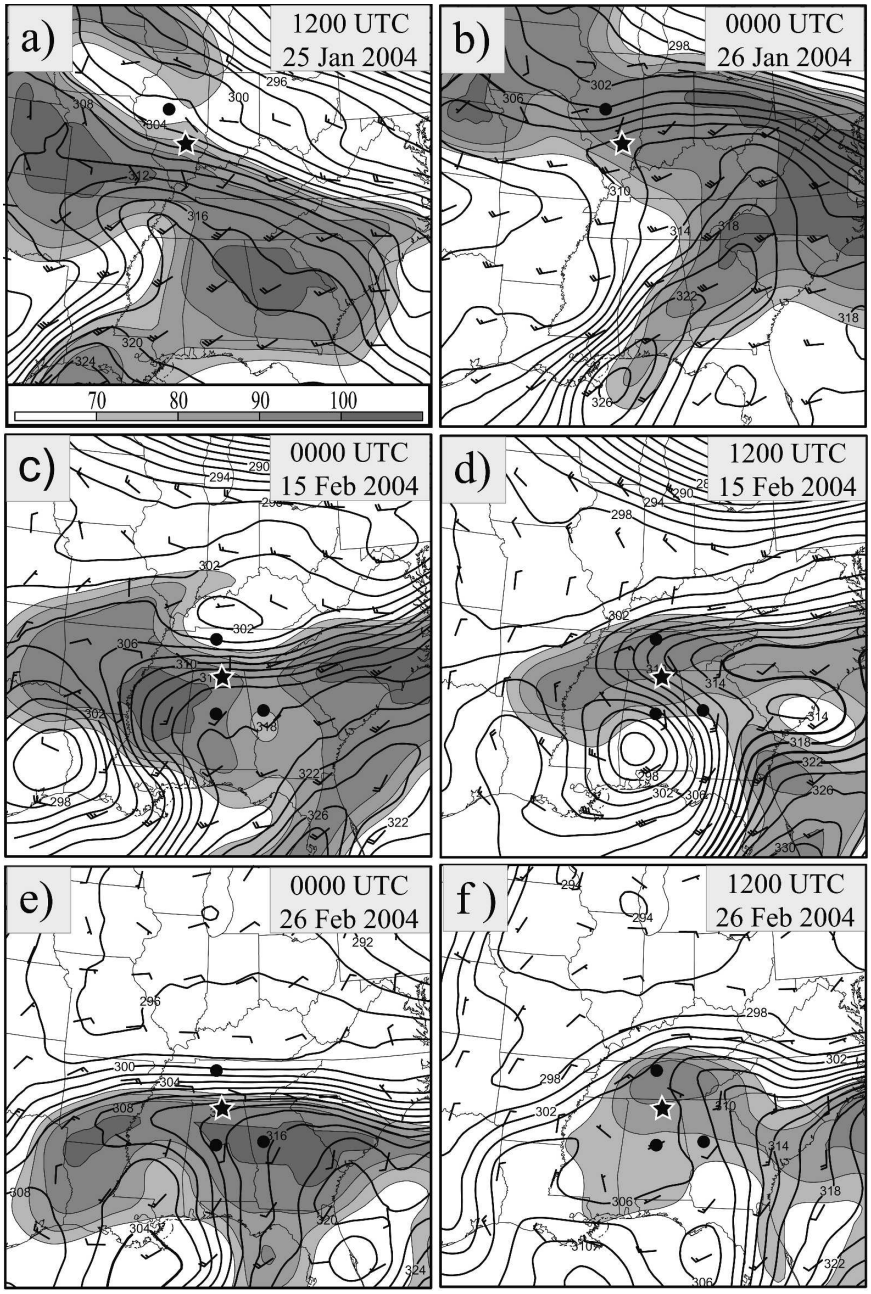

FIG. 6. As in Fig. 5, but for equivalent potential temperature.

a. C1, 25 January 2004, southern Illinois

The cyclone formed over Colorado around 0000 UTC 25 January 2004 and progressed southeastward into Oklahoma and Arkansas by 1200 UTC 25 January. Figures 5a,b and 6a,b depict the frontal structures associated with C1 at the 700-hPa level at 1200 UTC 25 January and 0000 UTC 26 January. The area sampled by the profiler was along a warm-frontal boundary that extended from Missouri through South Carolina at 1200 UTC and moved north of the Ohio River Valley by 0000 UTC. A region of high relative humidity was present along the warm front, which was coincident with the region of precipitation illustrated on the radar composite (Fig. 7a).

The precipitation began at the MIPS location in Flora at 1330 UTC as a series of bands passed over southern Illinois. The SNR profile during the precipitation event (1300–2200 UTC) revealed finescale bands that extended from the ground vertically to as high as 6

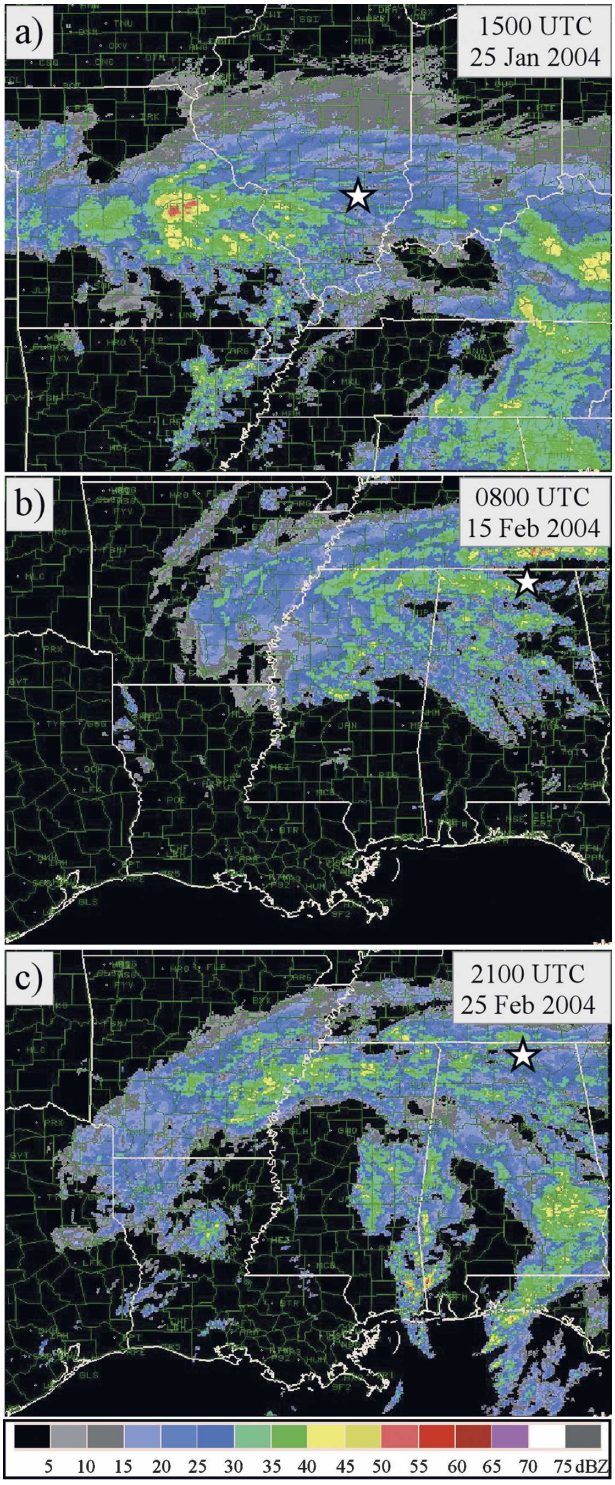

FIG. 7. Composite base reflectivity for (a) 1500 UTC 25 Jan 2004, (b) 0800 UTC 15 Feb 2004, and (c) 2100 UTC 25 Feb 2004. The star depicts the profiler location.

km (Fig. 8a). The bands ranged from approximately 5 to 35 km wide, were oriented roughly west to east, and moved northward at approximately 12 m s^{-1}. The melting level, apparent by relative maxima of SNR and a sharp gradient of radial velocity in Figs. 8a and 8b, respectively, was at 1.5 km for the first half of the precipitation event but rose to almost 2 km by 1900 UTC. The surface precipitation was in the form of freezing rain from 1330 through 1500 UTC and then turned to mixed rain and ice pellets. Between 1515 and 1545 UTC, a wide, elongated band passed over the profiler (band B). The precipitation at the surface during the passage of the band was entirely ice pellets. There was a lull in the precipitation around 1650 UTC, during which there was only a fine freezing drizzle, but light sleet resumed by 1700 UTC. The sleet alternated between light and heavy from 1730 through 1915 UTC before the precipitation stopped. Between 2000 and 2130 UTC, small drops of light freezing rain/drizzle mixed with small ice pellets fell intermittently. Approximately 3 mm (1/8 in.) of ice and 25 mm (1 in.) of sleet had accumulated during the 9-h period of precipitation at the profiler site in Flora.

A sounding launched at KILX at 1800 UTC during the passage of the bands over Lincoln (about 180 km northwest of the profiler) is representative of the band environment (Fig. 9a). The sounding showed an inversion up to 900 hPa, with a stable, saturated atmosphere through 450 hPa, the approximate top of the bands in Fig. 8a. By 0000 UTC 26 January, the precipitation had ended at the MIPS location.

b. C2, 15 February 2004, northern Alabama

This cyclone was associated with a weak surface low over Mississippi at 0000 UTC 15 February 2004. At this time at 700 hPa, a region of high relative humidity extended from Georgia westward into Arkansas (Figs. 5c and 6c). This region of moisture in which the bands formed was associated with a tongue of warm air—a feature termed the trough of warm air aloft, or trowal (see Martin 1998). The trowal progressively sharpened (Fig. 5d) during the period that the bands passed over the profiler in Huntsville (0300–1700 UTC 15 February, Fig. 8c).

Figures 9b and 9c show soundings taken at KBMX at 0000 UTC 15 February and KBNA at 1200 UTC 15 February. Both soundings were taken near the time that the profiled bands passed over these locations. At KBMX, a stable layer was present to the 850-hPa level, with a moist-adiabatic profile above that level. At KBNA, the atmosphere was dry and stable up to the 750-hPa level. Above that level, the temperature profile was moist adiabatic.

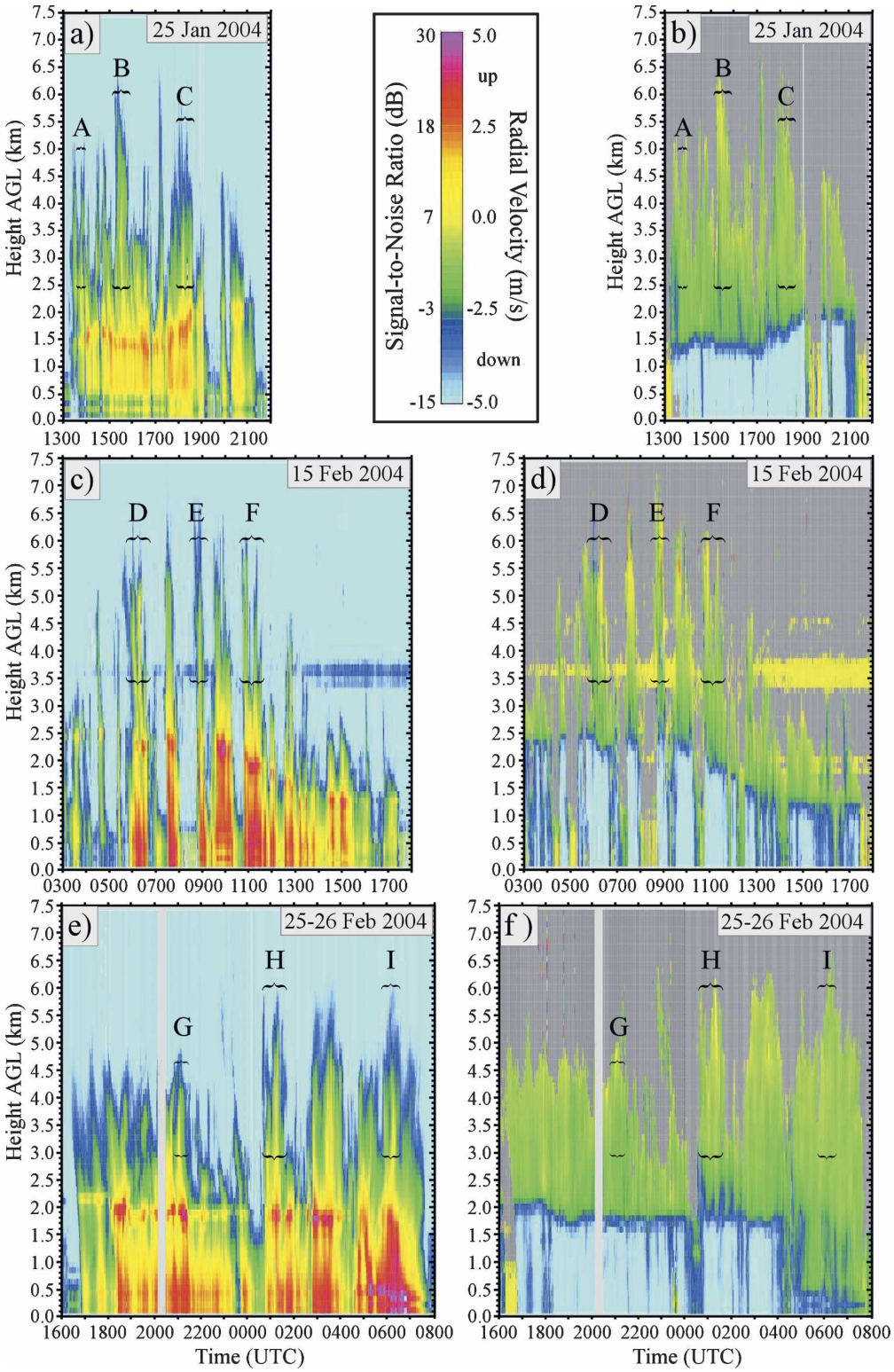

FIG. 8. Time series of 915-MHz Doppler wind profiler (left) SNR and (right) radial velocity above ground level for C1 at (a), (b) 25 Jan 2004 in Flora, for C2 at (c), (d) 15 Feb 2004 in Huntsville, and for C3 at (e), (f) 25–26 Feb 2004 in Huntsville. Key is shown in top center of figure. Negative values of radial velocity indicate motion toward profiler (downward). Lettered brackets correspond to the bands analyzed within each cyclone.

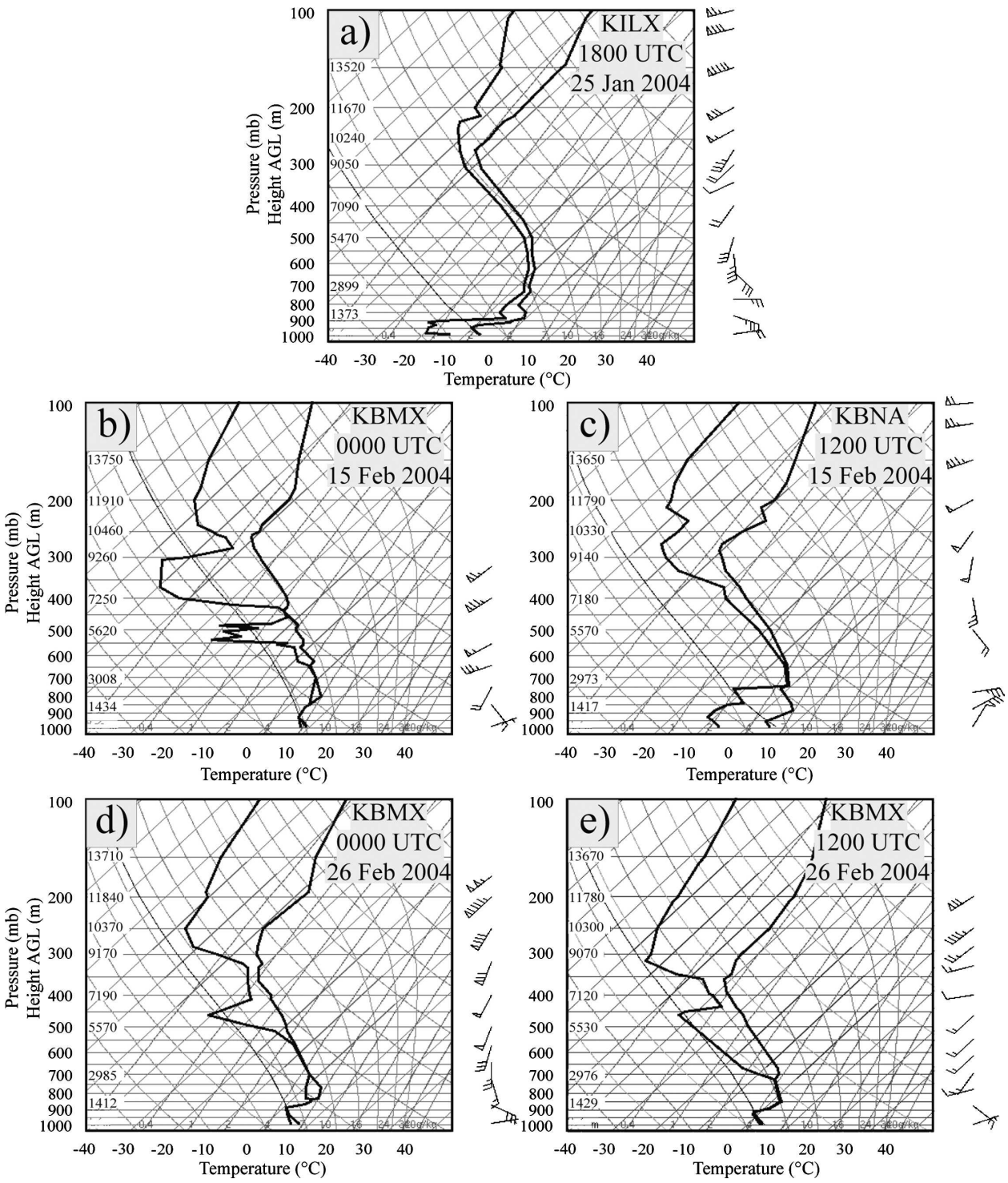

FIG. 9. Thermodynamic diagrams depicting soundings for C1 at (a) 1800 UTC 25 Jan 2004 taken from KILX, for C2 at (b) 0000 UTC 15 Feb 2004 taken from KBMX and (c) 1200 UTC 15 Feb 2004 taken from KBNA, and for C3 at (d) 0000 UTC 26 Feb 2004 and (e) 1200 UTC 26 Feb 2004 from KBMX.

The precipitation started as rain at about 0300 UTC in Huntsville. The bands between 0600 and 1200 UTC were 20–50 km wide and extended up to 6 km (Figs. 7b and 8c). Figures 5d and 6d show that by 1200 UTC the coldest/driest air at 700 hPa was positioned directly south of the MIPS location. At this time, the trowal was apparent over southern Tennessee and northern Alabama in the θ field. The precipitation changed to mixed rain, snow, and drizzle near 1200 UTC and continued as mixed precipitation until it ended at 1800 UTC. The melting level was around 2.5 km from 0300 through 1000 UTC, gradually decreasing to 1.25 km by 1300 UTC (Figs. 8c,d).

c. C3, 25–26 February 2004, northern Alabama

At 1200 UTC 25 February 2004, a weak surface low pressure system was located over the Gulf of Mexico, south of Alabama. The low formed along a preexisting cold front that had moved southward across the eastern United States. At 700 hPa, a band of moisture stretched along and over this frontal boundary (not shown).

By 2100 UTC 25 February, a narrow region of precipitation extended in an arc from northeast Texas, northeastward to northern Alabama, and then southeastward into Georgia along this moisture axis (Fig. 7c). A second area of precipitation extended along the Alabama–Mississippi border. Both areas of precipitation passed over the profiler during the event.

The area of precipitation along the arc reached the profiler location in Huntsville around 1700 UTC 25 February. Several narrow bands (10–35 km in width) produced rain as they passed over the profiler. The bands were 4–4.5 km deep between 1700 UTC 25 February and 0000 UTC 26 February (Fig. 8e). The mean orientation of the bands was from west to east as they moved north-northeastward (Fig. 7c). The height of the melting level was around 1.75 km during this time period (Figs. 8 e,f).

By 0000 UTC 26 February, the surface low had just moved onshore over southern Alabama. A trowal was present at 700 hPa from southeastern Arkansas through western Georgia (Figs. 5e). Although the moisture boundaries were sharp (Fig. 6e), the thermal gradients in this cyclone were weak at 700 hPa at 0000 UTC (Fig. 5e). Figure 9d shows the KBMX sounding for 0000 UTC 26 February. At this time a stable layer was present between 900 and 750 hPa, with a moist-adiabatic temperature profile between 750 and 450 hPa (the approximate top of the bands). Saturated air was present from 950 to 850 hPa and from 700 to 550 hPa, with dry air above.

The area of precipitation that was along the Alabama–Mississippi border at 2100 UTC (Fig. 7c) reached the profiler location around 0100 UTC 26 February. At this time, the bands changed characteristics in that they increased to 6 km in height and were approximately 30–60 km wide. Shortly after 0400 UTC 26 February, the height of the melting level fell abruptly to just under 0.5 km (Figs. 8e,f). The precipitation changed from rain to a mixture of rain and wet snow until it ended after 0800 UTC.

The low pressure system had shifted eastward and weakened by 1200 UTC 26 February, although a weak trowal structure was still present but was located from central Tennessee through South Carolina (Fig. 5f). The KBMX sounding showed a saturated layer from the ground up to 725 hPa and was dry above, with a stable layer between 925 and 850 hPa (Fig. 9e).

4. Vertical motions within the bands

Our goal was to determine the magnitudes of the vertical air motion within the precipitation bands. It is difficult to estimate accurately the terminal fall velocities of particles undergoing significant aggregation and melting as they approach the melting layer. Therefore, the calculations herein are limited to the layer extending from approximately 1 km above the melting level to the top of each band for each cyclone. In each case, we were interested in the vertical air motions at higher altitudes because the structure of the individual bands was most apparent at these altitudes (Fig. 8). The vertical air motions were deduced within the upper part of three bands in each cyclone (bands A–I in Fig. 8). The bands were chosen as a representative sample of all of the bands within each cyclone.

a. Cyclone C1

The vertical velocity w within bands A–C of C1 is contoured in Figs. 10a–c. The portion of the bands for which w was determined is outlined and overlaid on the SNR fields (Figs. 10d–f). Figures 11 and 12 are arranged similarly for bands D–F in C2 and bands G–I in C3, respectively. All heights in these and subsequent profiler figures are above ground level (AGL). Ground level is approximately 140 and 200 m above sea level in Flora and Huntsville, respectively.

Band A crossed the profiler in 19 min, corresponding to an approximate width of 7 km based on the average cross-band wind component within the layer for which w was calculated, in this case between 2.5 and 5.0 km. Values of vertical motion ranged from -1.4 to 3.3 m s^{-1} between 2.5 and 5.0 km (Fig. 10). Positive values of w were found throughout most of the band, with a mean updraft of 1.2 m s^{-1} (standard deviation $\sigma = 0.6$ m s^{-1}; see Table 2) and the highest values (1.5–3.3 m s^{-1})

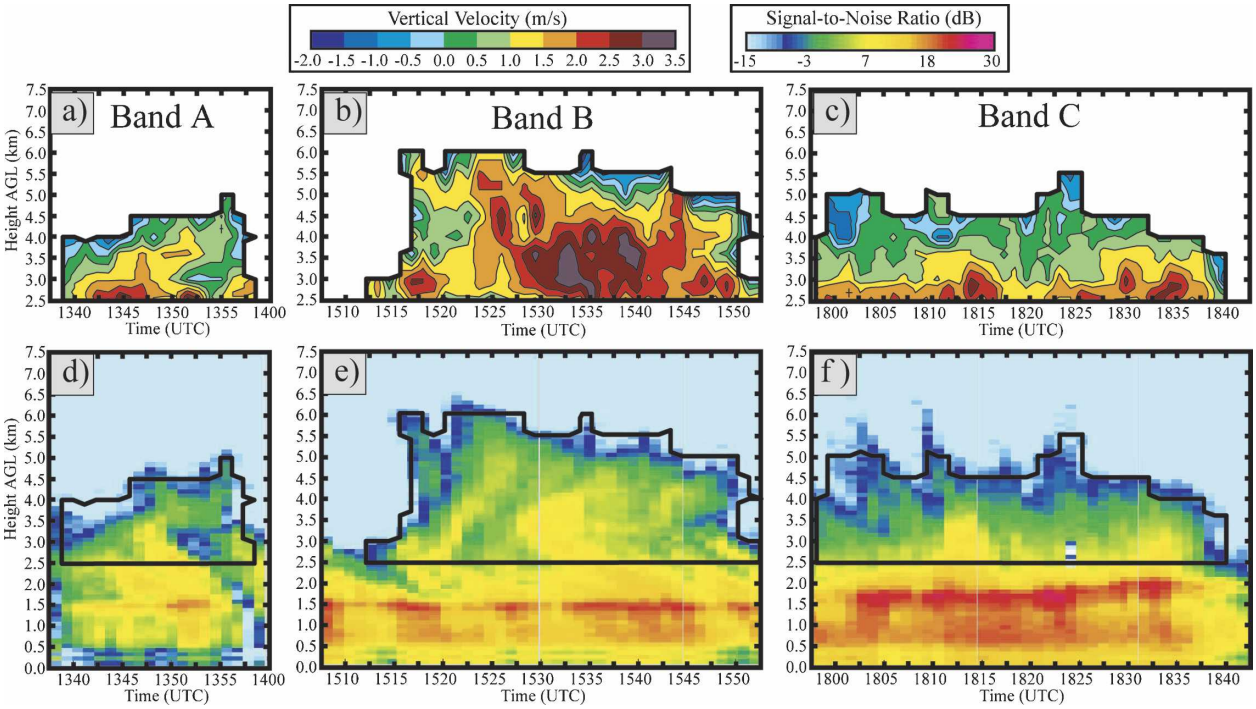

FIG. 10. Derived (top) vertical motion w and (bottom) SNR for three bands in C1 at (a), (d) 1340–1400; (b), (e) 1510–1550; and (c), (f) 1800–1840 UTC 25 Jan 2004. Outlined boxes in (d)–(f) show the areas of each band in which w was determined.

located between 2.5 and 3.5 km near the center. The regions of strongest positive vertical motion (updraft) generally corresponded to areas of high SNR (1.5–11 dB; Fig. 10d). Negative values of w averaged around -0.5 m s^{-1} ($\sigma = 0.3$ m s^{-1}), were found along the edges of the analysis area, and generally corresponded to the lowest values of SNR (from -3 to -15 dB).

Band B had an approximate width of 31 km and took about 39 min to pass over the profiler. Values of w ranged between -2.2 and 3.6 m s^{-1}. The mean upward velocity was 1.6 m s^{-1} ($\sigma = 0.8$ m s^{-1}). Figures 10b and 10e show that the strongest updrafts ($2.0 \leq w \leq 3.6$ m s^{-1}) were found within a widespread area near the center of the band between 2.5 and 4.5 km from

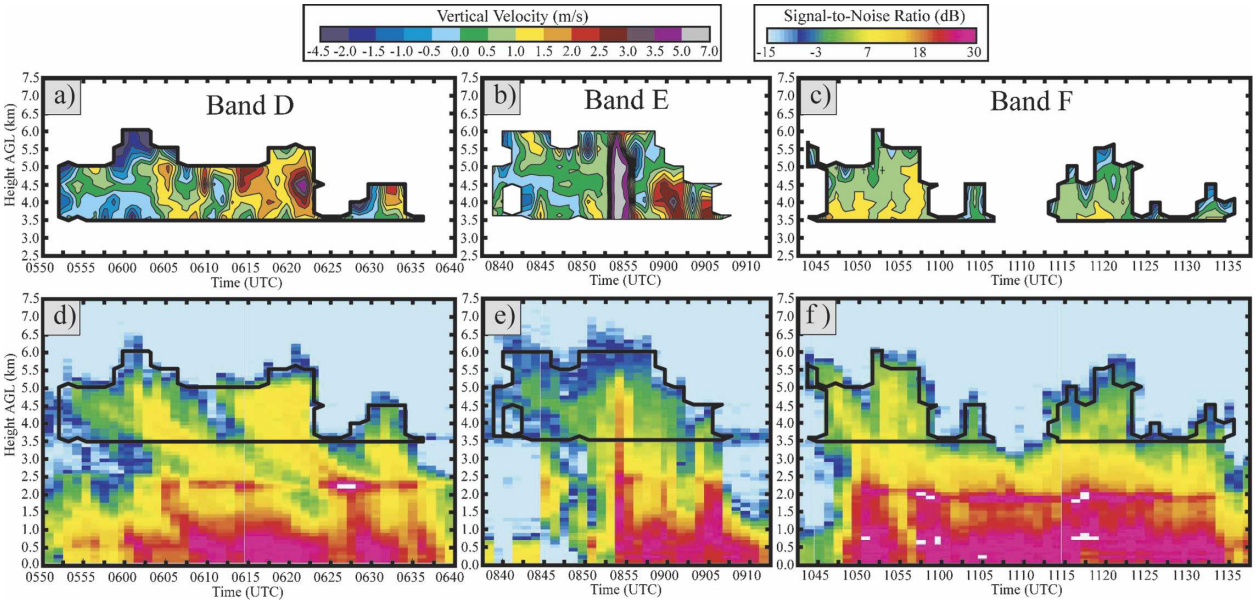

FIG. 11. As in Fig. 10, but for three bands in C2 at (a), (d) 0550–0640; (b), (e) 0840–0910; and (c), (f) 1045–1135 UTC 15 Feb 2004.

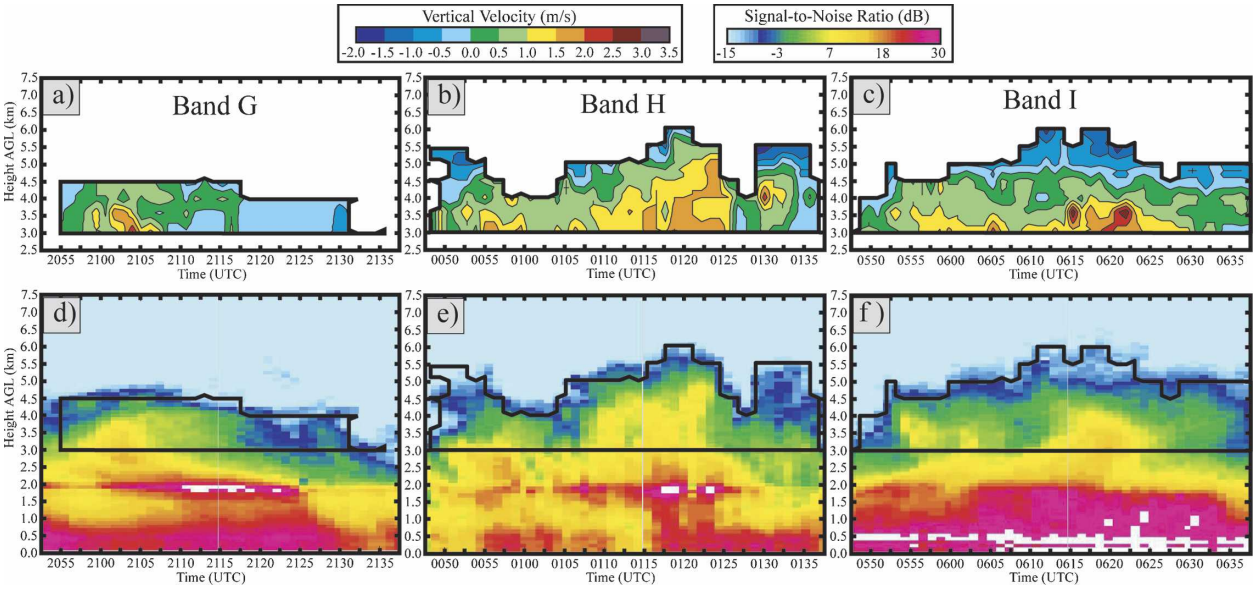

FIG. 12. Same as in Fig. 10, but for three bands in C3 at (a), (d) 2055–2135 UTC 25 Feb 2004, (b), (e) 0050–0135 UTC 26 Feb 2004, and (c), (f) 0550–0635 UTC 26 Feb 2004.

1530 to 1540 UTC, coinciding with the highest values of SNR (3–9 dB). Downdrafts ($-2.2 \leq w \leq -0.5$ m s^{-1}, average of -1.0 m s^{-1}, and $\sigma = 0.5$ m s^{-1}) were located along the edges of band B and were associated with regions of weak SNR (from -5 to -15 dB).

Band C passed over the profiler in a period of 41 min and was approximately 35 km wide. The range of vertical motion was from -1.9 to 2.9 m s^{-1} between 2.5 and 5.5 km (Fig. 10c). The average upward velocity was 1.0 m s^{-1} ($\sigma = 0.7$ m s^{-1}), with the strongest updrafts ($1.5 \leq w \leq 2.9$ m s^{-1}) between 2.5 and 3.5 km through the width of the band. Again, the regions of updrafts were coupled with regions of high SNR (2–10 dB) while the regions of stronger downdrafts ($w \leq -0.5$ m s^{-1}, average of -0.8 m s^{-1}, and $\sigma = 0.4$ m s^{-1}) were coupled with areas of weak SNR (from -3 to -15 dB; Fig. 10f) along the outer edges of the band.

In qualitative terms, a correlation between the values of SNR and vertical motion in Figs. 10a–f is evident. Figures 13a–d show a quantitative analysis of the correlation for bands A, B, and C and the overall correlation for C1. Bands A and C had the highest correlation coefficients r of 0.85, and band B had the lowest ($r = 0.76$). The correlation coefficient between all values of SNR and w within C1 was 0.79.

Figures 14a–d show cumulative frequency diagrams for w and the uncertainty in w (Δw) for each band within C1 and the overall analysis for C1. These diagrams show the percent of the total number of calculated values less than w. For example, Fig. 14a shows that 32% of the 83 samples for band A were negative (downdrafts), 43% were updrafts exceeding 1 m s^{-1}, and 7% exceeded 2.0 m s^{-1}. Only 14% of the 234 observations were negative in band B, 68% exceeded 1 m s^{-1}, and 25% exceeded 2.0 m s^{-1} (Fig. 14b). In band C, 16% of the 197 observations were negative, 37% exceeded 1 m s^{-1}, and 9% exceeded 2.0 m s^{-1} (Fig. 14c). Figure 14d shows that 17% of the 514 total observations for C1 were negative, over one-half (52%) were greater than 1 m s^{-1}, and 16% exceeded 2 m s^{-1}. The mean updraft (downdraft) velocity for C1 was 1.3 m s^{-1} (-0.8 m s^{-1}), with $\sigma = 0.8$ m s^{-1} (0.5 m s^{-1}). Table 2 summarizes the statistics for the analysis of the vertical motion in this cyclone, as well as for C2 and C3.

b. Cyclone C2

Band D, a combination of two narrow bands with little separation between them, had a total width of ~52 km and took 45 min to pass over the profiler. Values of w deduced between 3.5 and 6.0 km ranged from -4.3 to 4.3 m s^{-1} (Fig. 11a). The SNR field in Fig. 11d suggests that the two bands were sloped and that the tilted regions of strongest SNR (5–10 dB) corresponded to the regions of strongest updrafts ($1.5 \leq w \leq 2.9$ m s^{-1}; Fig. 11a). A small area of negative w (from 0 to -0.7 m s^{-1}) was located between the two narrow bands. Another region of downward motion (from 0 to -2 m s^{-1}) was located between 3.5 and 4.0 km from 0552 to 0605 UTC, coincident with the underside of the first tilted band. Negative values of w (from 0 to -4.3 m s^{-1}) were also found along the edges of the bands, consistent with the areas of weak SNR (from -4 to -15 dB). The mean

TABLE 2. Average values of w (m s^{-1}) and SNR–w correlation coefficient for each band, each cyclone, and all bands.

	A	B	C	D	E	F	G	H	I	C1	C2	C3	All
No. of w values	83	234	197	159	127	135	125	219	236	514	421	580	1515
Min w	−1.4 ± 0.6	−2.2 ± 0.6	−1.9 ± 0.6	−4.3 ± 0.8	−2.5 ± 0.8	−2.3 ± 0.6	−1.0 ± 0.4	−2.1 ± 0.6	−1.9 ± 0.6	−2.2 ± 0.6	−4.3 ± 0.7	−2.1 ± 0.6	−4.3 ± 0.6
Max w	3.3 ± 0.6	3.6 ± 0.6	2.9 ± 0.6	4.3 ± 0.8	6.7 ± 0.8	1.9 ± 0.6	2.7 ± 0.4	2.4 ± 0.6	3.0 ± 0.6	3.6 ± 0.6	6.7 ± 0.7	3.0 ± 0.6	6.7 ± 0.6
Mean positive w	1.2	1.6	1.0	1.2	1.5	0.8	0.6	0.9	0.8	1.3	1.1	0.9	1.1
Std dev positive w	0.6	0.8	0.7	0.8	1.6	0.4	0.5	0.5	0.5	0.8	1.1	0.5	0.9
Mean negative w	−0.5	−1.0	−0.8	−1.1	−0.7	−1.0	−0.3	−0.7	−0.7	−0.8	−1.0	−0.6	−0.7
Std dev negative w	0.3	0.5	0.4	1.0	0.7	0.6	0.2	0.5	0.4	0.5	0.8	0.4	0.6
Mean w	0.7	1.3	0.7	0.4	0.8	0.3	0.1	0.5	0.3	1.0	0.5	0.3	0.6
Std dev w	1.0	1.2	0.9	1.4	1.7	0.9	0.6	0.9	0.9	1.1	1.4	0.8	1.1
Correlation coef r	0.85	0.76	0.85	0.60	0.66	0.71	0.68	0.72	0.85	0.79	0.59	0.76	0.68

positive (negative) w was 1.2 m s^{-1}, with σ = 0.8 m s^{-1} (−1.1 m s^{-1}, with σ = 1.0 m s^{-1}).

Band E was approximately 33 km wide and took 28 min to cross the profiler (Fig. 11b). This band had the strongest updraft in the nine bands analyzed. The strongest updraft (6.7 m s^{-1}) took place in the center of the band between 0852 and 0856 UTC and corresponded directly with a small area of high SNR (10–17 dB; Fig. 11e). Values of w derived between 3.5 and 6.0 km ranged from −2.5 to 6.7 m s^{-1}. The mean updraft speed was 1.5 m s^{-1} (σ = 1.6 m s^{-1}) throughout the band, and the mean downdraft was −0.7 m s^{-1} (σ = 0.7 m s^{-1}). Regions of negative w (to −2 m s^{-1}) were found on the underside of the strong-echo region extending to the left side of the figure between 4 and 6 km from 0840 to 0850 UTC (Fig. 11b), with regions of weak upward motion (up to 1.5 m s^{-1}) within the echo region. In addition, downward motion was found along the edges of the band and also between two peaks in SNR and positive w between 0857 and 0907 UTC. Downdrafts correlated well with the regions of weak SNR (from −6 to −12 dB; Figs. 11b, e). Note that band E is unique in this dataset in that it can be classified as being convective based on the absence of a bright band in the SNR field, whereas the other bands appear to be more stratiform.

Band F consisted of two subbands that were only separated above 3.5 km (~1 km above the melting level, Fig. 11f). Band F passed over the profiler in 51 min, corresponding to a distance of about 58 km. Vertical motion between 3.5 and 6.0 km ranged from −2.3 to 1.9 m s^{-1}. The mean upward motion within band F was 0.8 m s^{-1} (σ = 0.4 m s^{-1}). Two regions of maximum updrafts (1.0–1.5 m s^{-1}) were present between 3.5 and 4.0 km near the center of each subband that corresponded to two regions of high SNR (2–7 dB). Downdrafts (from 0 to −2.3 m s^{-1}) were found along the edges of the band and were consistent with low values of SNR (from −5 to −15 dB; Figs. 11c, f). The mean negative w was −1.0 m s^{-1} (σ = 0.6 m s^{-1}).

Although there is an obvious correlation between SNR and w that is apparent in Figs. 11a–f, the correlation was not as strong as that in C1 (r_{C1} = 0.79). The overall correlation coefficient in C2 for all of the bands was 0.59 (Fig. 13h). Band D had the lowest correlation coefficient of 0.60, and band F had the highest at 0.71 (Figs. 13e–g).

Figures 14e–h show cumulative frequency diagrams of w and Δw for bands D–F and the overall analysis for C2. In band D, 35% of the 159 observations were negative, 39% exceeded 1 m s^{-1}, and 8% were greater than 2 m s^{-1} (Fig. 14e). Band E had a wide range of values of w, with 29% being negative, 34% being greater than 1 m s^{-1}, 19% being greater than 2 m s^{-1}, and 5% ex-

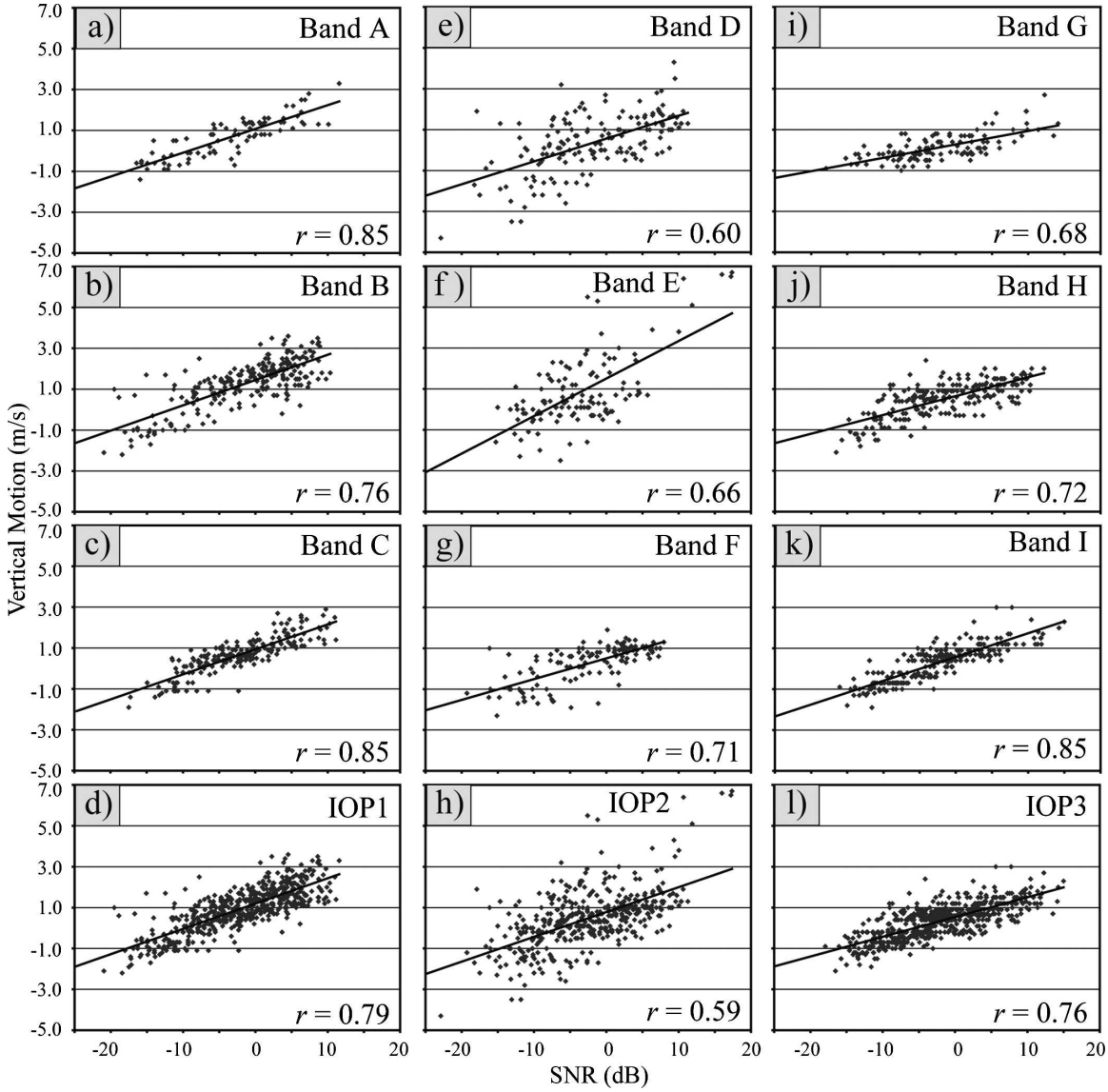

FIG. 13. Scatterplots of SNR vs derived vertical motion w for (a) band A in C1, (b) band B in C1, (c) band C in C1, (d) all bands in C1, (e) band D in C2, (f) band E in C2, (g) band F in C2, (h) all bands in C2, (i) band G in C3, (j) band H in C3, (k) band I in C3, and (l) all bands in C3. Solid line is linear regression line, with the correlation coefficient r in the lower corner of each figure.

ceeding 5 m s^{-1} (Fig. 14f). In a similar way, 28% of the values of w were negative in band F; however, there were no updrafts greater than 2 m s^{-1}, although 27% exceeded 1 m s^{-1} (Fig. 14g). Figure 14h shows that 31% of the 421 total observations during C2 were negative, 34% exceeded 1 m s^{-1}, and 9% exceeded 2.0 m s^{-1}. The mean positive updraft velocity for C2 was 1.1 m s^{-1} (σ = 1.1 m s^{-1}), and the mean downdraft velocity was −1.0 m s^{-1} (σ = 0.8 m s^{-1}).

c. Cyclone C3

Band G took 40 min to pass over the profiler and had an approximate width of 18 km. Values of w ranged between −1.0 and 2.7 m s^{-1} between 3.0 and 4.6 km (Fig. 12a), with an average updraft speed of 0.6 m s^{-1} (σ = 0.5 m s^{-1}). The strongest updraft (1.0–2.7 m s^{-1}) was located between 3.0 and 3.5 km from 2100 and 2105 UTC, toward the left side of the band (Fig. 12a), and matched up with the higher values of SNR (4–14 dB; Fig. 12d). This band contained a large area of negative w values (average of −0.3 m s^{-1}, with σ = 0.2 m s^{-1}), which correlated well with weak values of SNR (from −4 to −15 dB; Fig. 12d).

Band H took 48 min to pass over the profiler and had an approximate width of 38 km. The vertical motion ranged from −2.1 to 2.4 m s^{-1} between 3.0 and 6.0 km

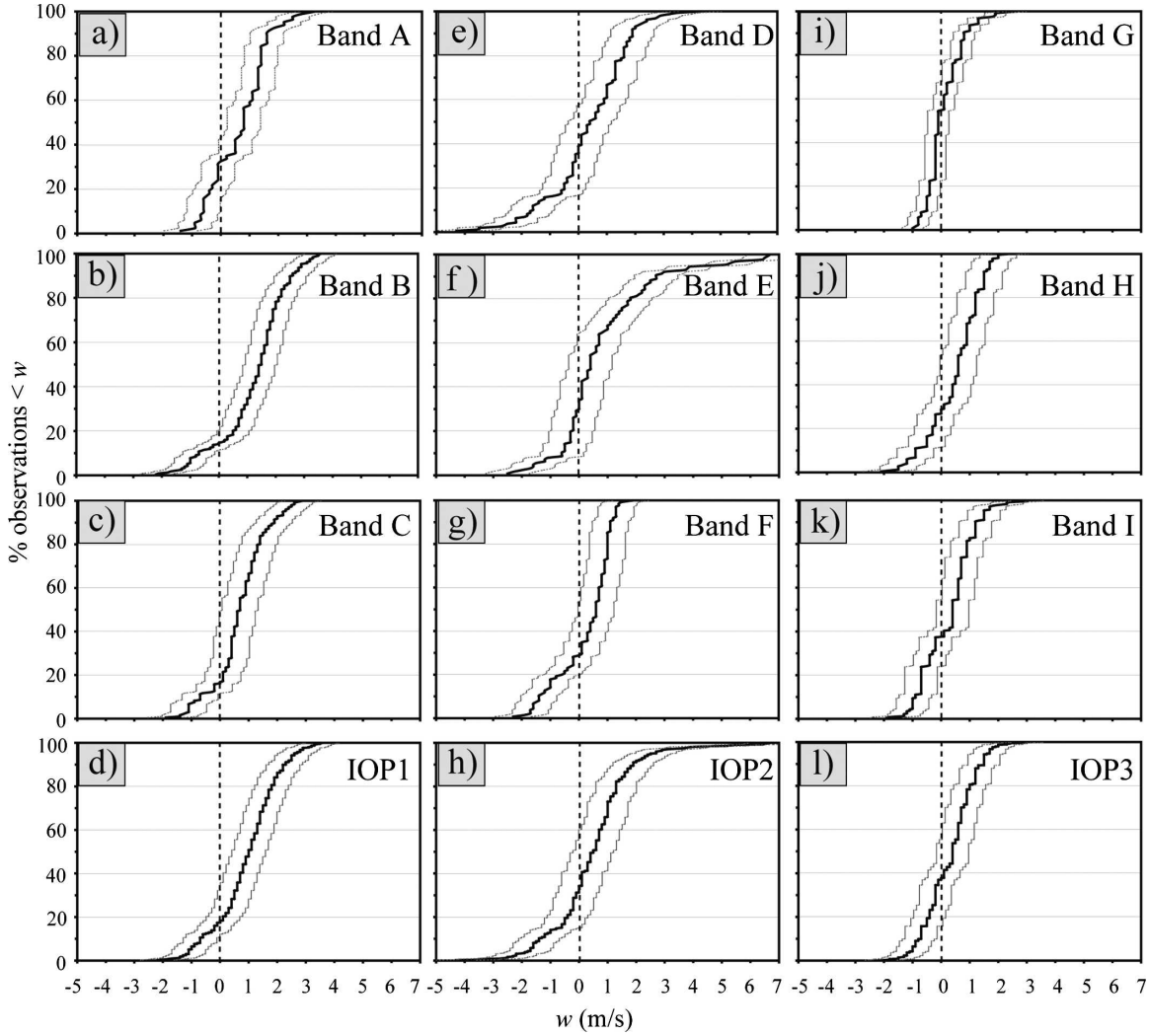

FIG. 14. Cumulative frequency diagrams showing the percent of derived w values less than w (center thick line in each panel) and the uncertainty in w (two thin lines in each panel) for (a) band A in C1, (b) band B in C1, (c) band C in C1, (d) all bands in C1, (e) band D in C2, (f) band E in C2, (g) band F in C2, (h) all bands in C2, (i) band G in C3, (j) band H in C3, (k) band I in C3, and (l) all bands in C3. Thick, vertical dashed line in each panel denotes the location of $w = 0$.

(Fig. 12b), with a mean updraft (downdraft) speed of 0.9 m s^{-1}, with $\sigma = 0.5$ m s^{-1} (-0.7 m s^{-1}, with $\sigma = 0.5$ m s^{-1}). There were two areas of maximum w (1.0–2.0 m s^{-1}) and corresponding maximum SNR (2–12 dB; Figs. 12 b,e); the first occurred from 0050 to 0100 UTC between 3.0 and 3.5 km toward the beginning of the band (left side of Fig. 12b), and the second was from 0110 to 0125 UTC and stretched up to 5.0 km in the last two-thirds of the band (right side of Fig. 12b). The downdrafts ($-2.1 \leq w \leq 0$ m s^{-1}) were mainly confined to the edge of the band and corresponded to regions of weak SNR (from -7 to -15 dB; Fig. 12e).

Figure 12c shows that band I took 50 min to pass and corresponded to a width of approximately 37 km. Its vertical velocities ranged between -1.9 and 3.0 m s^{-1} from 3.0 to 6.0 km, with the average positive w equal to 0.8 m s^{-1} ($\sigma = 0.5$ m s^{-1}). The maximum values of w (1.0–3.0 m s^{-1}) occurred between 3.0 and 4.0 km through the width of the band and were associated with regions of high SNR (1–15 dB), which is apparent in Fig. 12f. Downdrafts ($-1.9 \leq w \leq 0$ m s^{-1}, average of -0.7 m s^{-1}, and $\sigma = 0.4$ m s^{-1}) were located along the top edge of the band and correlated well with lower values of SNR (from -5 to -14 dB, Fig. 12f). Bands G–I in C3 all had very high correlations between SNR and w (Figs. 13i–l). The overall correlation coefficient for C3 was 0.76, with band I having the highest value ($r = 0.85$) and band G having the lowest ($r = 0.68$).

The cumulative frequency diagram of w and Δw in Fig. 14i shows that 55% of the w values were negative

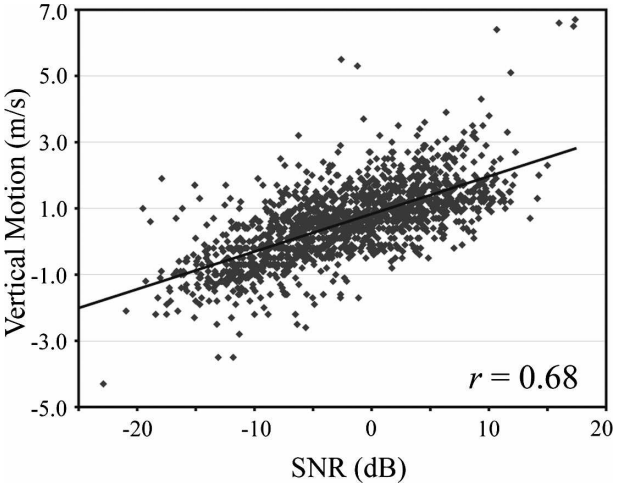

FIG. 15. Scatterplot of SNR vs derived vertical motion w for all cyclones combined. Solid line is linear regression. Correlation coefficient r is shown in the lower-right corner.

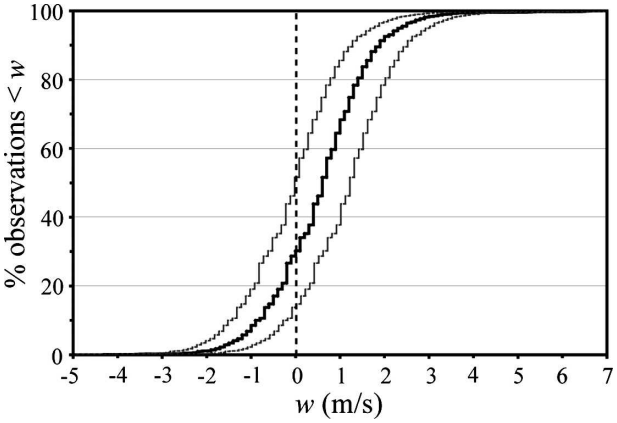

FIG. 16. Cumulative frequency diagram showing the percent of derived w values less than w (center thick line in each panel) and the uncertainty in w (two thin lines in each panel) for all cyclones combined. Thick, vertical dashed line denotes the location of $w = 0$.

in band G, 9% exceeded 1 m s^{-1}, and only 1% exceeded 2 m s^{-1}. In band H, 27% of the values of w were negative, 32% exceeded 1 m s^{-1}, and only 2% were greater than 2 m s^{-1} (Fig. 14j). In band I, 38% of values of w were below 0 m s^{-1}, 19% exceeded 1 m s^{-1}, and 3% were greater than 2 m s^{-1} (Fig. 14k). With the three bands combined in Fig. 14l, 37% of the 580 total derived values of w were negative, 22% exceeded 1 m s^{-1}, and 2% were greater than 2 m s^{-1}. The mean positive vertical motion for C3 was 0.9 m s^{-1} (σ = 0.5 m s^{-1}), and the mean downward motion was −0.6 m s^{-1} (σ = 0.4 m s^{-1}).

The correlation coefficient between the SNR and w for all nine bands in the three cyclones was 0.68 (Fig. 15). The cumulative frequency diagram for the overall analysis showed that 29% of the 1515 total derived values of w were negative, 35% exceeded 1 m s^{-1}, and 9% exceeded 2.0 m s^{-1} (Fig. 16). The minimum derived value of w was −4.3 m s^{-1} (in band D) and the maximum value was 6.7 m s^{-1} (in band E). The mean value of w for all cyclones was 0.6 m s^{-1}, with a standard deviation of 1.1 m s^{-1}, the mean upward vertical motion was 1.1 m s^{-1} (σ = 0.9 m s^{-1}), and the mean downward motion was −0.7 m s^{-1} (σ = 0.6 m s^{-1}). Table 2 summarizes these observations for all of the nine bands studied.

5. Summary

The goal of this study was to determine the magnitude of the vertical air velocities within precipitation bands in three winter cyclones. The cyclones occurred during January and February of 2004 over the midwestern and southern United States. The vertical air velocities were obtained from Doppler spectra measured by the vertical beam of the 915-MHz profiler mounted on the University of Alabama in Huntsville Mobile Integrated Profiling System using the lower-bound method, which in this paper was adapted to account for spectral broadening resulting from the mean horizontal wind, vertical shear of the horizontal wind, and turbulence. Vertical velocities were only derived between ~1 km above the melting level and the top of the bands. Within this layer, the fall velocities of the smallest detectable particles could be reliably estimated. Derived vertical air motions ranged from −4.3 to 6.7 m s^{-1}, with an uncertainty of about ±0.6 m s^{-1}. Approximately 29% of the 1515 total derived values of w were negative, 35% exceeded 1 m s^{-1}, and 9% exceeded 2.0 m s^{-1}. These values are generally somewhat larger than those found in previous studies in the Pacific Northwest. The ~6 m s^{-1} updraft observed in one band is much larger than any previously reported updraft in winter bands.

There was a high correlation between values of SNR and w within each band ($0.60 \leq r \leq 0.85$), in the composite of bands from each cyclone ($0.59 \leq r \leq 0.79$), and in the overall analysis (r = 0.68). The strongest updrafts were typically between 2.0 and 4.0 m s^{-1} and were typically located near the center of each band. These updrafts were usually found within regions of high SNR (5–15 dB). Regions of downdrafts within the bands had maximum values between −1.0 and −4.3 m s^{-1} and were typically located along the edges of the bands in regions of low SNR (from −5 to −15 dB). The prominence of downdrafts around the periphery of the bands is similar to the cloud-edge downdrafts noted for

convective clouds by Knupp and Cotton (1985, their Fig. 14) and Blyth et al. (1988, their Fig. 13). These results are consistent with snow growth and sublimation processes. As air ascends in an updraft, ice crystals grow larger, creating a stronger signal back to the profiler, which results in a higher SNR. Sublimation and cooling is expected along the edges of the bands, leading to sinking air and low values of SNR.

It was beyond the scope of this paper to determine the dynamical mechanism(s) forcing the bands in these three cyclones. We note, however, that the magnitudes of the vertical velocities in the core of the bands were comparable to, or exceeded, the theoretical predictions for moist symmetric instability under an assumption of an inviscid atmosphere (Emanuel 1983). Because tubes of air ascending slantwise in a sheared environment are likely to be disrupted by turbulent mixing (Emanuel 1983, p. 2372), it would appear that the larger of the retrieved vertical velocities in some bands exceeded those expected for moist symmetric instability. This suggests that other instabilities, such as potential instability, may have contributed to the vertical motion in some bands in these storms. High-resolution modeling studies, in conjunction with observations such as those presented here, are required in future investigations to determine the nature of the forcing unambiguously.

Acknowledgments. This work was supported by the National Science Foundation under Grants NSF-ATM0413824 and NSF-ATM0239889 and by a grant from the University of Illinois at Urbana–Champaign Research Board. The authors thank Professor Larry Di Girolamo for his assistance with this work.

APPENDIX

Analysis of Contributions from Bragg Scatter

For a 915-MHz radar, contributions to the total backscatter power (and hence to the Doppler spectrum) may arise both from Rayleigh scatter from raindrops and ice particles and from Bragg scatter associated with refractive index inhomogeneities. This issue has been analyzed in considerable detail by Gossard et al. (1992), Ralph (1995), and Williams et al. (2000). The ability of the LBM to retrieve vertical motion depends on the assumption that the Doppler spectra are produced only from Rayleigh scatter. Bragg scatter contributions, if present, would produce a positive bias in vertical motion values retrieved with the LBM. In the following, we show that contributions from Bragg scatter are indeed negligible for the cases examined.

For Rayleigh scattering, the radar reflectivity is given as

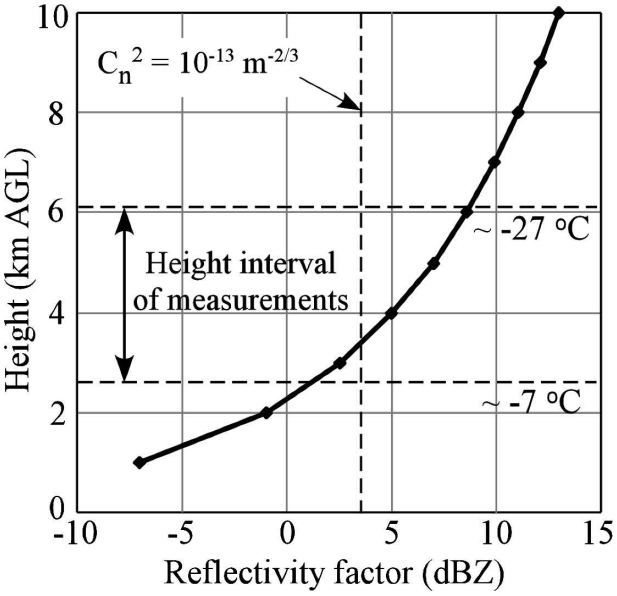

FIG. A1. Minimum detectable reflectivity factor vs height for the MIPS 915-MHz profiler. The height range of measurements is indicated, and the dBZ value (3.5) corresponding to $C_n^2 = 10^{-13}$ m$^{-2/3}$ is marked by the vertical dashed line.

$$\eta = \pi^5 |K|^2 \lambda^{-4} \sum_{\text{vol}} D^6, \tag{A1}$$

where $\Sigma_{\text{vol}} D^6$ is the radar reflectivity factor Z for a unit volume.

For Bragg scatter, the radar reflectivity is proportional to the refractive index structure function C_n^2 through the relation

$$C_n^2 = (\lambda^{1/3}/0.38)\eta. \tag{A2}$$

Combining Eqs. (A1) and (A2) defines the association between Z and C_n^2 as

$$Z = 0.38\lambda^{11/3}\pi^{-5}|K|^{-2}C_n^2. \tag{A3}$$

Thus, C_n^2 is an important parameter that will describe the contribution from Bragg scatter (Gossard et al. 1992; Ralph 1995; Williams et al. 2000). Ralph (1995) determined that extreme and high threshold values of C_n^2 are 10^{-13} and 10^{-15} m$^{-2/3}$, respectively. Data compiled by Chadwick and Moran (1980) indicate that the 10^{-13} m$^{-2/3}$ *extreme value* is exceeded in only about 0.5% of their observations of boundary layer turbulence. According to Eq. (A3), the corresponding Z values are 3.5 and −16.5 dBZ, respectively. Figure A1 presents the minimum detectable Z versus height for the 915-MHz wind profiler used in this study. It is based on a calibration within rain using disdrometer data during June of 2003. (We further note that a weakening amplifier very likely increased the minimum detectable

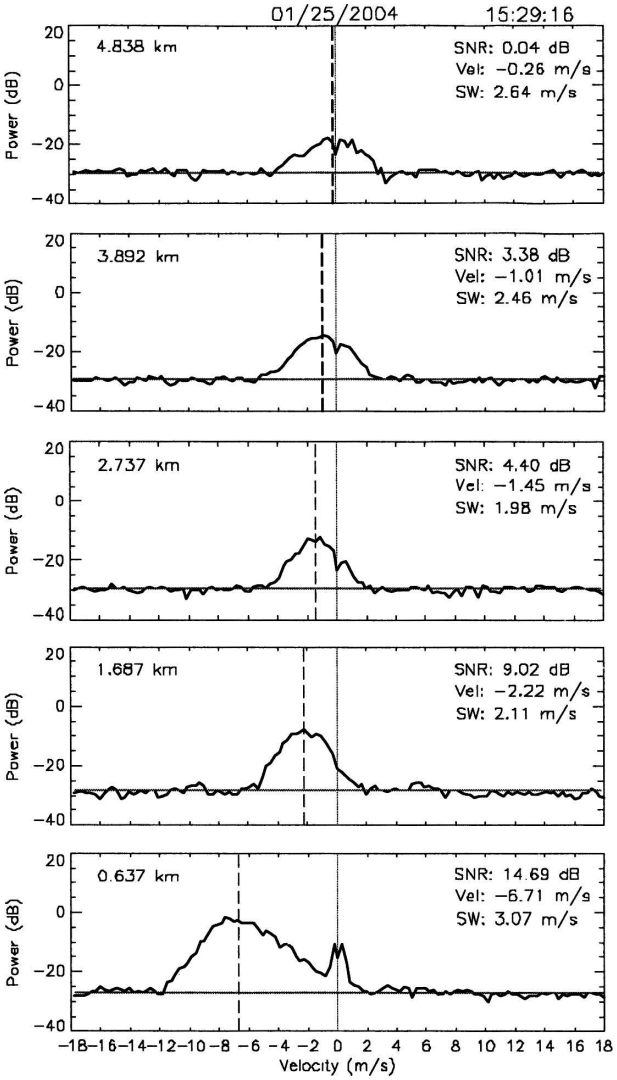

FIG. A2. Profile of spectra for an updraft at 1529 UTC 25 Jan 2004.

Z during the PlOWS study period.) The height and temperature ranges of the measurements considered in this paper are also indicated in Fig. 1, along with the Z value (3.5 dBZ) corresponding to the extreme value of $C_n^2 = 10^{-13}$ m$^{-2/3}$, using Eq. (A3). It is apparent that the contribution from Bragg scatter is not likely for significant turbulence ($C_n^2 = 10^{-13}$ m$^{-2/3}$). Inspection of values of the spectrum width σ_w for each case considered in this paper reveals maximum values of 1.5–2 m s^{-1}, implying low values of turbulence. Such values are in the range of σ_w values (0.5–2.5 m s^{-1}) within the stratiform region of tropical mesoscale convective systems (Williams et al. 1995). This corroborates that C_n^2 within stratiform precipitation is typically much less than 10^{-13} m$^{-2/3}$ within the cloud systems studied.

Close examination of the Doppler spectra used herein offers supporting evidence that Bragg scatter does not contribute to spectral density above 2.5 km AGL. In specific terms,

1) no signal was detected just before the onset of precipitation in the 25 January case, even though cloud was present (as detected by the microwave profiling radiometer),
2) the spectra within the 2.5–7.0 km AGL layer (Fig. A2) typically display a symmetric structure, with no asymmetry that could be ascribed to Bragg scatter, and
3) the cloud system samples are cold ($-27°\text{C} < T < -7°\text{C}$), stable, and horizontally extensive. The latter feature would imply that entrainment is not a significant issue. The general pattern of weak downdrafts on cloud edges is contrary to a positive bias in w that would be produced by the presence of Bragg scatter.

REFERENCES

Atlas, D., 1964: Advances in radar meteorology. *Advances in Geophysics,* Vol. 10, Academic Press, 318–478.

——, R. C. Srivastava, and R. S. Sekhon, 1973: Doppler radar characteristics of precipitation at vertical incidence. *Rev. Geophys. Space Phys.,* **11,** 1–35.

Battan, L. J., 1973: Turbulence spreading of Doppler spectrum. *J. Appl. Meteor.,* **12,** 822–824.

——, and J. B. Theiss, 1966: Observations of vertical motions and particle sizes in a thunderstorm. *J. Atmos. Sci.,* **23,** 78–87.

Bennetts, D. A., and B. J. Hoskins, 1979: Conditional symmetric instability—A possible explanation for frontal rainbands. *Quart. J. Roy. Meteor. Soc.,* **105,** 945–962.

——, and J. C. Sharp, 1982: The relevance of conditional symmetric instability to the prediction of mesoscale frontal rainbands. *Quart. J. Roy. Meteor. Soc.,* **108,** 595–602.

Bluestein, H. B., 1993: *Synoptic-Dynamic Meteorology in Midlatitudes.* Vol. 2, *Observations and Theory of Weather Systems,* Oxford University Press, 594 pp.

Blyth, A. M., W. A. Cooper, and J. B. Jensen, 1988: A study of the source of entrained air in Montana cumuli. *J. Atmos. Sci.,* **45,** 3944–3964.

Chadwick, R. B., and K. P. Moran, 1980: Long-term measurements of C_n^2 in the boundary layer. *Radio Sci.,* **15,** 355–362.

Donaldson, R. J., Jr., and R. Wexler, 1969: Flight hazards in thunderstorms determined by Doppler velocity variance. *J. Appl. Meteor.,* **8,** 128–133.

Emanuel, K. A., 1983: The Lagrangian parcel dynamics of moist symmetric instability. *J. Atmos. Sci.,* **40,** 2368–2376.

Foote, G. B., and P. S. du Toit, 1969: Terminal velocity of raindrops aloft. *J. Appl. Meteor.,* **8,** 249–253.

Geerts, B., and P. V. Hobbs, 1991: Organization and structure of clouds and precipitation on the mid-Atlantic coast of the United States. Part IV: Retrieval of the thermodynamic and cloud microphysical structures of a frontal rainband from Doppler radar data. *J. Atmos. Sci.,* **48,** 1287–1305.

Gossard, E. E., R. G. Strauch, D. C. Welsh, and S. Y. Matrosov, 1992: Cloud layers, particle identification, and rain-rate profiles from ZRVf measurements by clear-air Doppler radars. *J. Atmos. Oceanic Technol.,* **9,** 108–119.

Hertzman, O., and P. V. Hobbs, 1988: The mesoscale and microscale structure and organization of clouds and precipitation in midlatitude cyclones. Part XIV: Three-dimensional airflow and vorticity budget of rainbands in a warm occlusion. *J. Atmos. Sci.,* **45,** 893–914.

——, ——, and J. D. Locatelli, 1988: The mesoscale and microscale structure and organization of clouds and precipitation in midlatitude cyclones. Part XVI: Three dimensional airflow and vertical vorticity budget for a warm front. *J. Atmos. Sci.,* **45,** 3650–3666.

Herzegh, P. H., and P. V. Hobbs, 1980: The mesoscale and microscale structure and organization of clouds and precipitation in midlatitude cyclones. II: Warm-frontal clouds. *J. Atmos. Sci.,* **37,** 597–611.

——, and ——, 1981: The mesoscale and microscale structure and organization of clouds and precipitation in midlatitude cyclones. IV: Vertical air motions and microphysical structures of prefrontal surge clouds and cold-frontal clouds. *J. Atmos. Sci.,* **38,** 1771–1784.

Hobbs, P. V., T. J. Matejka, P. H. Herzegh, J. D. Locatelli, and R. A. Houze Jr., 1980: The mesoscale and microscale structure and organization of clouds and precipitation in midlatitude cyclones. I: A case study of a cold front. *J. Atmos. Sci.,* **37,** 568–596.

Houze, R. A., Jr., S. A. Rutledge, T. J. Matejka, and P. V. Hobbs, 1981: The mesoscale and microscale structure and organization of clouds and precipitation in midlatitude cyclones. III: Air motions and precipitation growth in a warm-frontal rainband. *J. Atmos. Sci.,* **38,** 639–649.

Innocentini, V., and E. dos Santos Caetano Neto, 1992: A numerical study of the role of humidity in the updraft driven by moist slantwise convection. *J. Atmos. Sci.,* **49,** 1092–1106.

Knight, D. J., and P. V. Hobbs, 1988: The mesoscale and microscale structure and organization of clouds and precipitation in midlatitude cyclones. Part XV: A numerical modeling study of frontogenesis and cold-frontal rainbands. *J. Atmos. Sci.,* **45,** 915–930.

Knupp, K. R., and W. R. Cotton, 1985: Convective cloud downdraft structure—An interpretive survey. *Rev. Geophys.,* **23,** 183–215.

Locatelli, J. D., and P. V. Hobbs, 1974: Fallspeeds and masses of solid precipitation particles. *J. Geophys. Res.,* **79,** 2185–2197.

——, and ——, 1987: The mesoscale and microscale structure and organization of clouds and precipitation in midlatitude cyclones. XIII: Structure of a warm front. *J. Atmos. Sci.,* **44,** 2290–2309.

Martin, J. E., 1998: The structure and evolution of a continental winter cyclone. Part II: Frontal forcing of an extreme snow event. *Mon. Wea. Rev.,* **126,** 329–348.

Nicosia, D. J., and R. H. Grumm, 1999: Mesoscale band formation in three major northeastern United States snowstorms. *Wea. Forecasting,* **14,** 346–368.

Novak, D. R., L. F. Bosart, D. Keyser, and J. S. Waldstreicher, 2004: An observational study of cold season–banded precipitation in the northeast U.S. cyclones. *Wea. Forecasting,* **19,** 993–1010.

Passarelli, R. E., Jr., 1978: Theoretical and observational study of snow-size spectra and snowflake aggregation efficiencies. *J. Atmos. Sci.,* **35,** 882–889.

Persson, P. O. G., and T. T. Warner, 1995: The nonlinear evolution of idealized, unforced, conditional symmetric instability: A numerical study. *J. Atmos. Sci.,* **52,** 3449–3474.

Probert-Jones, J. R., and W. G. Harper, 1961: Vertical air motions in showers as revealed by Doppler radar. *Proc. Ninth Weather Radar Conf.,* Boston, MA, Amer. Meteor. Soc., 225–232.

Ralph, F. M., 1995: Using radar-measured radial vertical velocities to distinguish precipitation scattering from clear-air scattering. *J. Atmos. Oceanic Technol.,* **12,** 257–267.

Rauber, R. M., M. K. Ramamurthy, and A. Tokay, 1994: Synoptic and mesoscale structure of a severe freezing rain event: The St. Valentine's Day ice storm. *Wea. Forecasting,* **9,** 183–208.

Reuter, G. W., and M. K. Yau, 1990: Observations of slantwise convective instability in winter cyclones. *Mon. Wea. Rev.,* **118,** 447–458.

Rogers, R. R., S. G. Leblanc, S. A. Cohn, W. L. Ecklund, D. A. Carter, and J. S. Wilson, 1996: Profiler measurements of turbulence and wind shear in a snowstorm. *Beitr. Phys. Freien Atmos.,* **69,** 27–36.

Sanders, F., 1986: Frontogenesis and symmetric stability in a major New England snowstorm. *Mon. Wea. Rev.,* **114,** 1847–1862.

——, and L. F. Bosart, 1985: Mesoscale structure in the Megalopolitan snowstorm, 11–12 February 1983. Part II: Doppler radar study of the New England snowband. *J. Atmos. Sci.,* **42,** 1398–1407.

Schultz, D. M., and P. N. Schumacher, 1999: The use and misuse of conditional symmetric instability. *Mon. Wea. Rev.,* **127,** 2709–2732.

Seltzer, M. A., R. E. Passarelli, and K. A. Emanuel, 1985: The possible role of symmetric instability in the formation of precipitation bands. *J. Atmos. Sci.,* **42,** 2207–2219.

Sienkiewicz, J. M., J. D. Locatelli, P. V. Hobbs, and B. Geerts, 1989: Organization and structure of clouds and precipitation on the mid-Atlantic coast of the United States. Part II: The mesoscale and microscale structures of some frontal rainbands. *J. Atmos. Sci.,* **46,** 1349–1364.

Thorpe, A. J., and K. A. Emanuel, 1985: Frontogenesis in the presence of small stability to slantwise convection. *J. Atmos. Sci.,* **42,** 1809–1824.

Wang, P.-Y., and P. V. Hobbs, 1983: The mesoscale and microscale structure and organization of clouds and precipitation in midlatitude cyclones. X: Wavelike rainbands in an occlusion. *J. Atmos. Sci.,* **40,** 1950–1964.

——, D. B. Parsons, and P. V. Hobbs, 1983: The mesoscale and microscale structure and organization of clouds and precipitation in midlatitude cyclones. VI: Wavelike rainbands associated with a cold-frontal zone. *J. Atmos. Sci.,* **40,** 543–558.

Williams, C. R., W. L. Ecklund, and K. S. Gage, 1995: Classification of precipitating clouds in the Tropics using 915-MHz wind profilers. *J. Atmos. Oceanic Technol.,* **12,** 996–1012.

——, ——, P. E. Johnston, and K. S. Gage, 2000: Cluster analysis techniques to separate air motion and hydrometers in vertical incident profiler observations. *J. Atmos. Oceanic Technol.,* **17,** 949–962.

Wolfsberg, D. G., K. A. Emanuel, and R. E. Passarelli, 1986: Band formation in a New England winter storm. *Mon. Wea. Rev.,* **114,** 1552–1569.

Xu, Q., 1992: Formation and evolution of frontal rainbands and geostrophic potential vorticity anomalies. *J. Atmos. Sci.,* **49,** 629–648.

Zhang, D.-L., and H.-R. Cho, 1995: Three-dimensional simulation of frontal rainbands and conditional symmetric instability in the Eady-wave model. *Tellus,* **47A,** 45–61.